NTNU

Norwegian University of
Science and Technology

Solidification of Titanium Slags and Influence on Post Processing

Rune Hagberg Stana

Materials Science and Engineering
Submission date: June 2016
Supervisor: Leiv Kolbeinsen, IMTE
Co-supervisor: Stian Seim, TiZir Titanium & Iron

Norwegian University of Science and Technology
Department of Materials Science and Engineering

Preface

This thesis is written as a part of my Master's Degree at the Norwegian University of Science and Technology (NTNU), Department of Materials Science and Engineering. It is written as a part of the research project SFI Metal Production.

This work is done in collaboration with the industrial plant Tizir Tianium & Iron in Tyssedal, Norway.

I would like to thank my supervisor Professor Leiv Kolbeinsen. You have been a good weekly discussion partner, providing valuable insights in many fields, be it relevant or not.

Secondly, I would like to thank Professors Merete Tangstad, Gabriella Tranell and Ragnhild Aune for the work put in through the SiManTi research group. Thanks to all the members of the group as well: our weekly meetings promotes discussions around many approaches to materials research.

The research team at Tizir Tyssedal have been very helpful regarding sample collection, analyses and discussions. Thank you to Haavard Elstad, Arne Hildal, Stian Seim and Stephen Lobo.

For practical help at the university, I would like to thank Michal Ksiazek and Dmitry Slizovskiy for aiding me in conducting my experiments.

June 2016
Rune Hagberg Stana

Abstract

Ilmenite is a titanium-rich ore, and accounts for almost all the world's consumption of titanium bearing minerals. One of the main uses of titanium is as powdered TiO_2, used extensively as whitening pigment. The first step in the process of making TiO_2 pigment, is reducing the ilmenite to a titanium-rich slag.

The titanium slag consists mainly of a titanium phase on the form of M_3O_5. The elements Fe, Mn and Mg can substitute Ti in the M_3O_5 lattice, and the slag also contains impurities such as SiO_2, CaO, Al_2O_3, Cr_2O_3 and V_2O_5. The slag needs to be purified and processed to make the pigment end product. This thesis focuses on the stage after reducing the ilmenite to a titanium-rich slag, and before the further purification of the slag.

To get a better understanding of the properties of the solid slag after reduction in the blast furnace, both industrially collected and experimentally prepared samples have been analyzed. It is believed that the cooling rate and access to oxygen of the slag during solidification will influence the microstructure of the solidified slag. This gives rise to differences in both grain size and shape, as well as the phases present.

Samples were collected from the industrial plant Tizir Titanium & Iron in Tyssedal, Norway. Slag samples prepared at the university were made by controlling temperature during solidification, and the properties of the samples were linked to those of the slags from the industrial plant.

Slag cross-sections were analyzed using BSD images and EDS spectra from the electron microscope. Phases in the slags were analyzed with X-ray diffraction. A theoretical review of thermal analysis for the slags was conducted.

The main titanium phases identified were pseudobrookite and rutile. The samples that experience slow cooling yielded a higher amount of rutile than the other samples. These samples also exhibited generally larger pseudobrookite grains. The experimentally produced samples were concluded to all have experienced cooling rates faster than those collected industrially.

Further work includes preparing samples with both solidification rates and other conditions closer to those of the industrial process. Another step is continued work on accurately measuring thermal properties of the slags, as this is an important parameter both to the industrial process as well as a quantitative measurement separating the different slag samples.

Table of Contents

List of Figures

Chapter 1

Introduction

1.1 Ilmenite

The major mineral source for titanium is ilmenite. It accounts for roughly 91% of the world's consumption of titanium bearing minerals [11]. The name ilmenite refers to both the chemical compound $FeTiO_3$, and natural ores consisting mainly of this compound.

The ilmenite ore is usually found in igneous rocks associated with magnetite, Fe_3O_4. The ore itself often contains hematite, Fe_2O_3, as well as a plethora of impurities. The main ones are Mg and Mn which substitute Fe in the $FeTiO_3$ lattice. Other major impurities are SiO_2, CaO, Al_2O_3, Cr_2O_3 and V_2O_5.

The amounts of impurities depends on the deposit the ore originates from. There are two types of ilmenite deposits: sand and rock deposits. Sand deposits are usually weathered over time, leading to many impurities being washed out. This results in a higher purity ore. Rock deposits do not experience this effect, which makes them higher in impurities. Differences in impurities can affect the processing chain of the ore. There are only two major utilized rock deposits (the Tellnes mine in Norway and the Lac Allard mine in Canada), while sand deposits are numerous. TiZir Titanium & Iron has historically utilized ilmenite from Tellnes, Norway, but is now using ore from the Grand Cte mine in Senegal.

1.2 Titanium processing

1.2.1 Ilmenite smelting

Ilmenite smelting was originally patented by Quebec Iron & Titanium Corporation (QIT) in 1949. The process involves carbonaceous reduction of ilmenite in an electric arc furnace. The furnace is fed with ilmenite and carbon in the form of coal, coke or char. The materials melt and ilmenite is reduced to metallic iron and tetravalent titanium, as shown in Equation 1.1. Tetravalent titanium is also partially reduced to trivalent titanium according to Equation 1.2 [12].

$$FeTiO_3(l) + C(s) \rightarrow Fe(l) + TiO_2(l) + CO(g) \tag{1.1}$$

$$TiO_2(l) + C(s) \rightarrow Ti_2O_3(l) + CO(g) \tag{1.2}$$

The furnace contains a liquid metal phase and a liquid slag phase. The phases separate because of differences in densities and can be tapped from different holes. The iron is sold as a high purity pig iron, while the slag is used as a feedstock to the pigment industry.

1.2.2 The Becher process

The Becher process is named after Robert Becher who published his works on the subject in 1965 [1]. The first step of the Becher process is solid state reduction of the ilmenite. Ilmenite and coal are fed to a rotary kiln operating at $1100\,^{\circ}\mathrm{C}$. The coal reacts to form CO gas as seen in Equation 1.3. The CO gas is the reducing agent when producing metallic iron, as shown in Equation 1.4.

$$C(s) + CO_2 \rightarrow 2CO(g) \tag{1.3}$$

$$FeTiO_3(s) + CO(g) \rightarrow Fe(s) + TiO_2(s) + CO_2(g) \tag{1.4}$$

The metallised ilmenite is then leached with water, ammonium chloride and air to dissolve Fe^{2+} in the water. The iron precipitates in the aerated solution as $Fe(OH)_2$, leaving behind the solid TiO_2. This synthetic rutile is further leached with sulphuric acid to remove remaining iron and manganese impurities. An overview of the Becher Process is shown in Figure 1.1.

The Becher process yields a high purity TiO_2 slag, but no metallic iron product.

1.2.3 The Tyssedal Process

The Tyssedal process is a combination of conventional ilmenite smelting and the Becher process. The ilmenite is first prereduced in the same way as the solid state reduction in the Becher process. In the Tyssedal process, about 70% of the iron in the ilmenite is prereduced to metallic iron. This product is then fed to an electric arc furnace similar to the conventional ilmenite smelting. An overview of the total Tyssedal process is shown in Figure 1.2.

The slag is tapped to large wagons, creating slag cakes of 7 to 10 tons. The cakes are cooled for $3\,\mathrm{h}$ on the wagons before they are handled and left to cool under a water spray.

The Tyssedal process produces a high titania slag and a high purity pig iron.

1.2.4 Pigment production

The titanium rich slags produced in the processes described above have to be further processed to be used as TiO_2 pigment. There are two primary processes for this: the sulphate process and the chloride process [13].

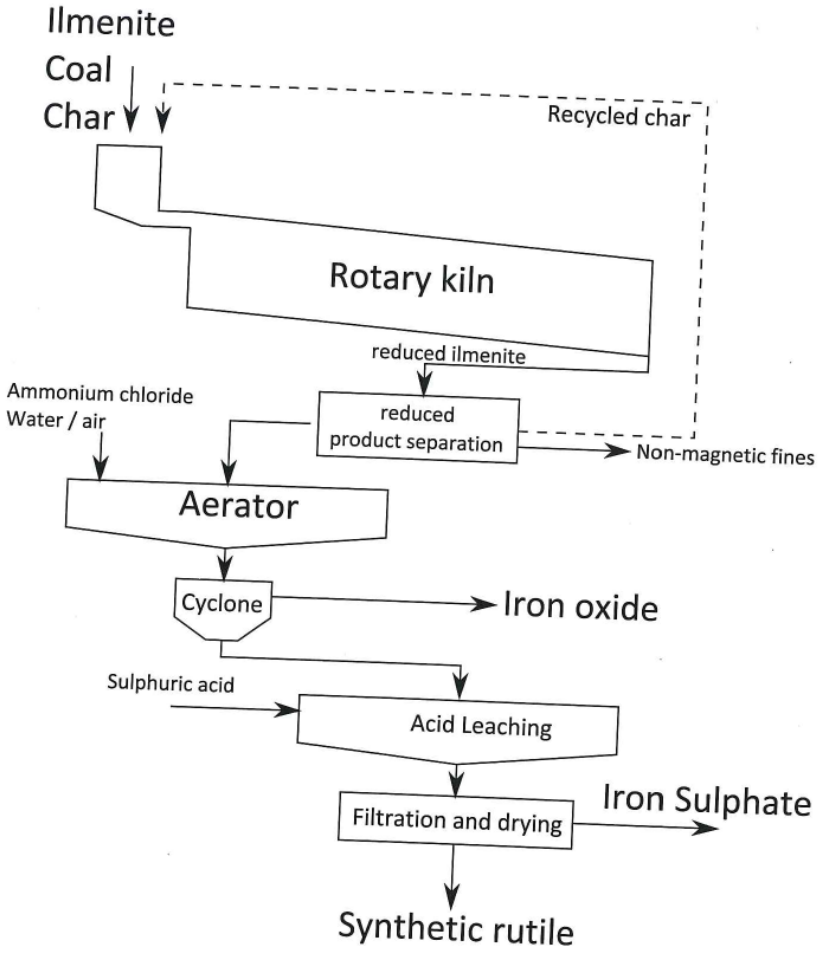

Figure 1.1: The Becher Process as described by [1] and drawn by [2]

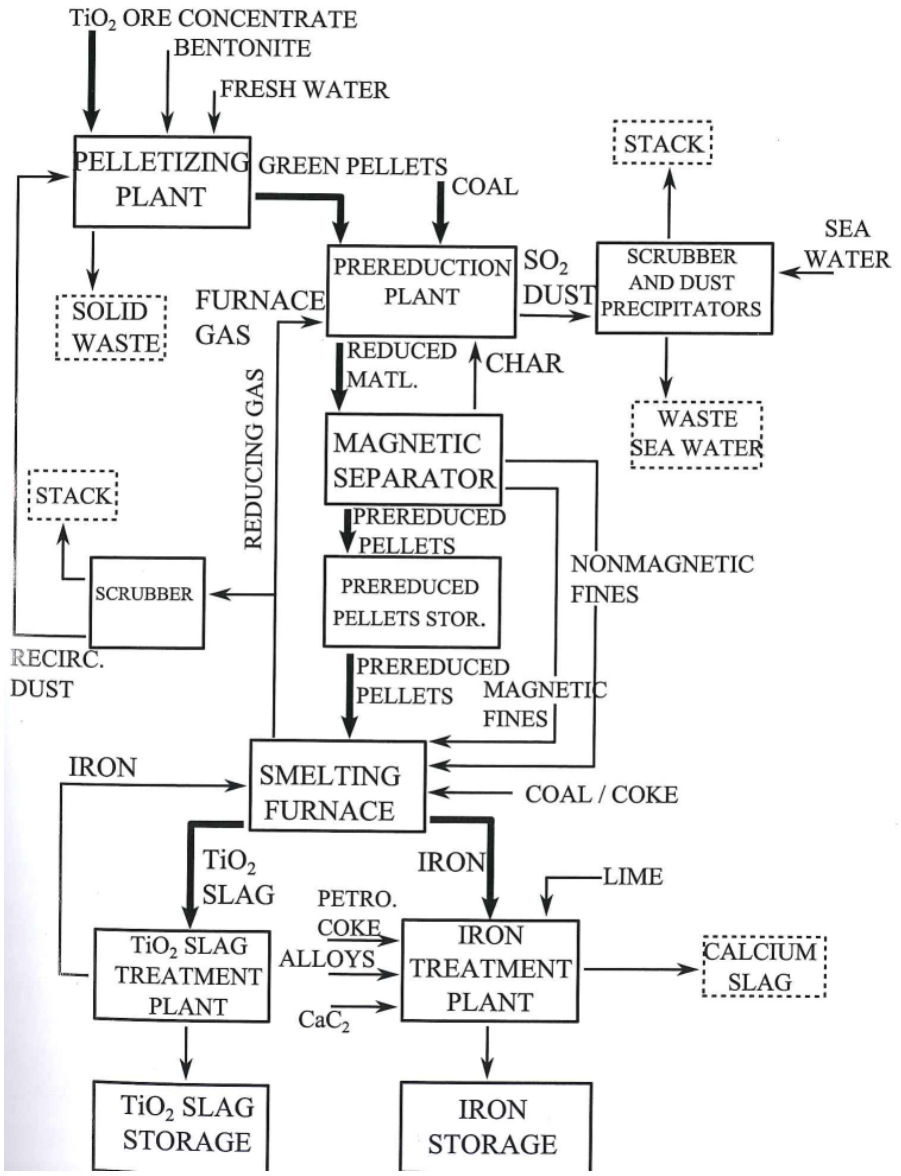

Figure 1.2: The Tyssedal Process as described by [3] and drawn by [2]

In the sulphate process, the ground slag is ingested with strong sulphuric acid. First, $FeSO_4$ is crystallized from the solution, then TiO_2 is precipitated as fine white pigment.

As rutile is not soluble in sulphuric acid, any rutile in the slag will produce a final product. The sulphate process can handle many impurities in the slag feedstock, and is generally used for low quality slags. It does, however, produce a large amount of by-products.

In the chloride process, slag, chlorine gas and coke is mixed in a fluidized bed reactor. Gaseous titanium tetrachloride ($TiCl_4$) is formed in the reactor. The $TiCl_4$ is condensed to a liquid while impurities separate as solids. The $TiCl_4$ liquid is reheated to gaseous form together with oxygen, producing a very pure TiO_2 pigment and chlorine gas [14].

Because of the impurities separating as solids in the reactor, this process requires a very pure slag. Specifically, the MgO and CaO impurities may not be higher than 1.5 and 0.5 wt%, respectively. The nature of the fluidized gas process requires the crushed slag feedstock to be of very specific size. The slag particles must be between $850\,\mu m$ and $106\,\mu m$.

1.3 Objective and outline of this thesis

The objective of this thesis is to characterize the microstructural properties of an industrial slag from Tyssedal. The cooling rate of the slag during solidification is of importance, and the samples used cover a wide range of cooling rates. Samples collected both industrially and prepared at the university is analyzed.

The end goal of studying the microstructure of the slag is to provide an extensive understanding of how changes to the cooling process will affect mechanical properties of the slag during crushing. The reason for this is the specific particle size imposed by the chloride production process, as previously described. This is, however, not within the scope of this thesis.

Chapter 2

Basic Theory

2.1 Thermal properties

2.1.1 Conductivity and diffusivity

The exchange of heat is divided into three different mechanisms: convection, radiation and conduction. This work will only use the conduction mechanism. Thermal conduction is the transfer of heat through a material due to a temperature gradient. Heat is transferred from hot to cold, acting to equalize temperature differences.

Heat conductivity of a material is a property of the material indicating it's ability to transfer heat through conduction. Conductivity is explained in the following way by ***R.B. Bird*** [15]:

A solid slab of thickness Y and area A is placed between two large parallel plates. Initially both plates are held at a constant temperature T_0, so the slab is also at T_0. At the time $t = 0$ the lower slab is brought to, and maintained at, the temperature $T_1 > T_0$. The temperature profile in the slab will initially change over time until it reaches a steady-state condition. At the steady-state a constant rate of heat flow Q through the slab is required to maintain the temperature difference $\Delta T = T_1 - T_0$. The following equation holds for small ΔT:

$$\frac{Q}{A} = \lambda \frac{\Delta T}{Y} \tag{2.1}$$

The heat flow rate per unit area is proportional to the temperature decrease of distance. λ is the constant of proportionality, and is termed the *conductivity* of the material. By taking $q_y = \frac{Q}{A}$ and reducing the slab thickness infinitesimally close to zero, Equation 2.2 is produced. This is the heat flow in positive y-direction, hence the negative.

$$q_y = -\lambda \frac{dT}{dy} \tag{2.2}$$

With a temperature gradient in all directions, Equation 2.2 can be expanded in all three coordinate directions:

$$q_x = -\lambda \frac{dT}{dx} \qquad q_y = -\lambda \frac{dT}{dy} \qquad q_z = -\lambda \frac{dT}{dz} \tag{2.3}$$

Adding the equations together after multiplying with the appropriate unit vector creates Equation 2.4.

$$q = -\lambda \nabla T \tag{2.4}$$

This is the three dimensional form of Fourier's law. This describes the conductive transfer of heat in an isotropic media.

Another value commonly used in addition to the thermal conductivity λ, is the thermal *diffusivity* α, as defined in Equation 2.5.

$$\alpha = \frac{\lambda}{\rho C_p} \tag{2.5}$$

ρ is the density and C_p is the heat capacity of the material at constant pressure.

2.1.2 Expansion

Most solid materials will react to heating and cooling by expanding and contracting, respectively. Thermal expansion can be defined as the change of any dimensional parameter with respect to temperature. Equation 2.6 describes linear thermal expansion.

$$\begin{aligned} \frac{l_f - l_0}{l_0} &= \alpha_l (T_f - T_0) \\ \frac{\Delta l}{l_0} &= \alpha_l \Delta T \end{aligned} \tag{2.6}$$

In this equation, l_0 and l_f describe the initial and final lengths with the temperature change from T_0 to T_f. The parameter α_l is the linear coefficient of thermal expansion. In other words, it describes how much the material expands when heated.

2.1.3 Specific heat

When a solid material is heated, it experiences an increase in temperature. Heat capacity explains the relationship between added heat and resulting temperature increase. It is defined as follows, where the second line is the infinitesimal version of the first:

$$\begin{aligned} C &= \frac{Q}{\Delta T} \\ C &= \frac{dQ}{dT} \end{aligned} \tag{2.7}$$

The concept of heat capacity requires a temperature increase with added heat, it is therefore not used together with phase transformations or chemical reactions.

When measuring heat capacity, either the specimen volume or the external pressure is maintained constant. The heat capacity at constant volume (C_P) and constant pressure (C_V) is shown in equation 2.8.

$$\begin{aligned} C_V &= (\frac{\delta Q}{dT})_V \\ C_P &= (\frac{\delta Q}{dT})_P \end{aligned} \tag{2.8}$$

Heat capacity at constant pressure (C_P) is an extensive property, while C_V is not. Because of this, C_P is convenient to use per quantity in the system. This is called the *molar heat capacity* when given per mole, and called the *specific heat capacity* when given per unit mass.

Material	Copper (C11000)	Steel (A36)	Al_2O_3 (99.9% pure)	Glass (soda-lime)
Conductivity [W/mK]	388	51.9	39	1.7
Thermal expansion [$10^{-6}/°C$]	17.0	11.7	7.4	9.0
Specific heat [J/kgK]	385	486	775	840

Table 2.1: Thermal properties of some reference materials. Compiled from [16]

.

2.2 Characterization methods

2.2.1 EDS analysis

Energy-dispersive X-ray spectroscopy (EDS) is a technique used in the scanning electron microscope (SEM) for qualitative and quantitative element analysis in the phases present in a sample.

The incoming electron beam is aimed at a specific area on the sample. The high-energy electron beam will excite inner shell electrons in the sample atoms, producing a secondary electron as well as a hole in the electron shell. An electron from a higher energy shell will fall into the generated hole, releasing an X-ray in the process.

The energy of the released X-ray is decided by the difference in energy levels between the two electron shells, which is specific to the element they belong to. EDS analysis measures the energy of the released characteristic X-rays to form a spectrum as shown in Figure 2.1. The number of each specific X-ray detected is used to generate a quantitative reading of the sample chemistry [17].

EDS is poor at analyzing the light elements (Z $<$11). Oxygen will be present in many of the phases to be analyzed, so the actual quantitative analysis of oxygen should not be trusted to be correct.

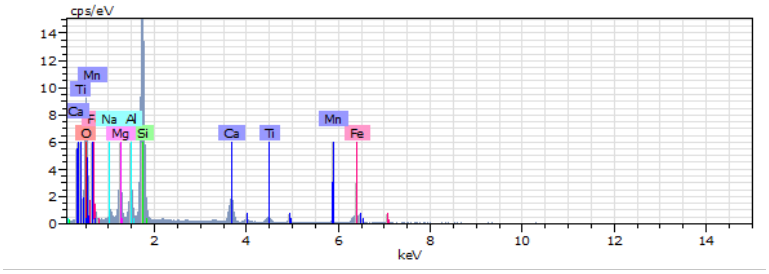

Figure 2.1: EDS generated X-ray spectrum

2.2.2 BSE imaging

Back-scattered electron (BSE) imaging is a technique used to get clear images of a sample surface, where different phases are contrasted by their difference in chemistry.

The back-scattered electrons are electrons originating in the primary electron beam down on the sample. The electrons will ”bounce off” after elastic collision with atoms in the sample. Atoms of higher numbers in the periodic system have a higher probability of intercepting the primary electrons, making them generate more back-scattered electrons than lower numbered atoms.

Back-scattered electrons can escape from the sample even from a small distance below the sample surface. Because of this, the BSE imaging technique does not give a precise picture of the specific sample surface. Studying the surface can be done by a variety of other techniques.

2.2.3 XRD analysis

X-ray diffraction (XRD) is a technique used to identify the crystallographic structure of a sample.

Monochromatic X-rays are generated by accelerating an electron beam through a high voltage down onto a target material. The target material is, in most cases, a piece of copper. The X-ray is generated in the same way as the signal used for EDS analysis, but in this case the primary X-ray is only of a single energy state: the K_α X-ray.

The generated X-ray beam is guided to the sample. The crystallographic planes in the sample phases will diffract the beam. These crystallographic planes behave as semi-transparent mirrors which will cause the diffracted beam to emit positive interference when Bragg’s Law (Equation 2.9) is satisfied.

$$2dsin(\theta) = n\lambda \tag{2.9}$$

d is the distance between pairs of adjacent planes, θ is the angle of incidence and λ is the wavelength of the incoming X-ray beam. For a given set of planes, several solutions of Bragg’s law are usually possible, for $n = 1, 2, 3$. It is customary to set n equal to one [18].

By tilting the sample, the angle of incidence is changed. By analysing the strength of the resulting diffracted beam, a spectrum is generated. This can be checked against tabulated values for known crystals, which in turn reveals the structures in the sample.

2.2.4 Laser Flash

Principle of the method

The laser flash method is a characterization method to analyze the properties *thermal diffusivity*, *thermal conductivity* and *specific heat capacity* of a sample.

A schematic drawing of the procedure is shown in Figure 2.2a. The principle of the method is as follows:

The power source heats the bottom surface of the sample with a short energy pulse. The temperature increase on the upper surface of the sample is measured using an infrared detector. The temperature of the sample chamber is controlled by the heating elements together with a thermocouple next to the sample. This is used to get readings as a function of temperature. A reference sample of known thermal properties is measured together with the sample in question.

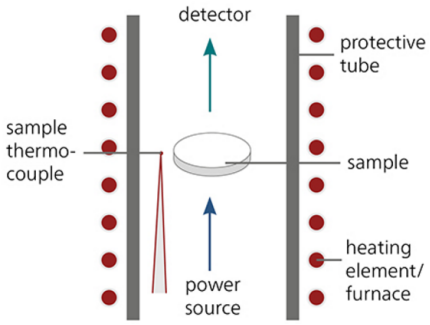

(a) Laser Flash principle [4]

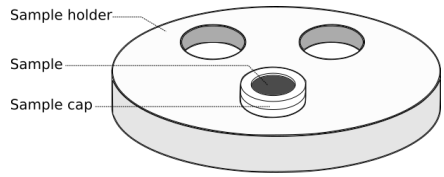

(b) Sample arrangement

Figure 2.2: Laser flash principle and sample arrangement

If the thickness, density and thermal expansion of the sample is known, the properties previously mentioned can be calculated.

Figure 2.3 shows the temperature reading of the sample over a few seconds after the energy pulse hits the lower side of the sample [4]. The maximum temperature increase (ΔT_{max}) in Equation 2.10 is the temperate of the sample after stabilizing.

$$\Delta T_{max} \propto \frac{1}{m * C_P} \tag{2.10}$$

$$a = 0.1388 \frac{d^2}{t_{1/2}} \tag{2.11}$$

$$\lambda(T) = a(T) * C_p(T) * \rho(T) \tag{2.12}$$

The half-time, time before $\frac{1}{2}\Delta T_{max}$ is reached, is used to calculate the variable a with Equation 2.11. The thermal conductivity is then calculated using Equation 2.12. The step-by-step process is shown in Figure 2.3.

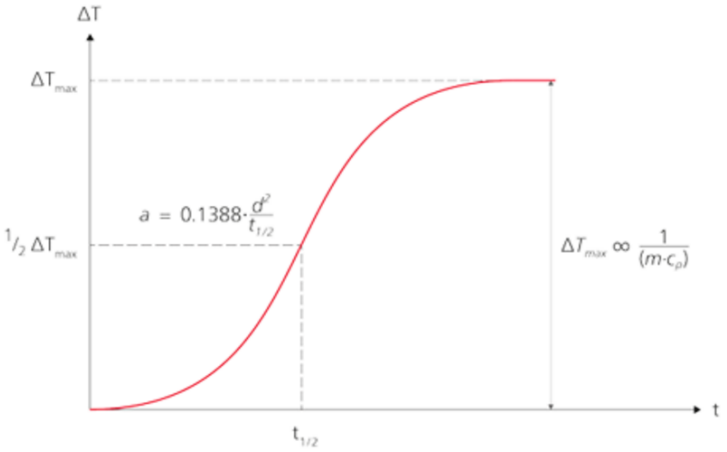

Figure 2.3: Temperature reading after a laser flash pulse [4]

Since the amount of heat absorbed in the sample and the reference sample are equal, the specific heat capacity of the sample can be calculated. This requires that the heat capacity of the reference sample is known.

Heat capacity can be expressed as:

$$C_P = \frac{Q}{m\Delta T} \tag{2.13}$$

and since the absorbed energies are equal:

$$Q_A = (mC_P\Delta T)_{ref} = (mC_P\Delta T)_{sample} \tag{2.14}$$

the specific heat capacity of the sample can be expressed as:

$$C_{Psample} = \frac{(mC_p\Delta T)_{ref}}{(m\Delta T)_{sample}} \tag{2.15}$$

Sample requirements

The main requirement for samples when doing laser flash thermal analysis is to obtain uniform heat absorption and heat radiation from the sample bottom and top surfaces, respectively. The first step for obtaining this is to cover the surfaces of the samples with a thin carbon layer.

According to [19] non-uniform heating of the sample can occur if the sample is too thin. A sufficiently thick sample is expressed as:

$$\frac{L}{2r} \geq 1 \tag{2.16}$$

where L is the thickness and r is the radius of the sample. According to this publication, the non-uniform heating effect is most significant when $0.15 < \frac{L}{2r} < 0.3$. As will later be explained in Section 4.3, the samples used in this thesis has a diameter for $12.7\,\mathrm{mm}$ and a width of approximately $2\,\mathrm{mm}$. This places the $\frac{L}{2r}$ size specification inside the area of dangers of non-uniform heating. The titanium slags being analyzed in this work has a low thermal conductivity, and samples considerably thicker than $2\,\mathrm{mm}$ will conduct heat too slow from the bottom to top surface to get good readings.

2.3 Slag structure

2.3.1 Phases present

The microstructure of the solidified high-titania slag is dominated by a titanium-rich M_3O_5 phase [20]. The other phases present are small amounts of rutile (TiO_2), metallic iron and a silicate glass phase. The glassy silicate phase contains most of the impurities of the slag, and is found between the larger M_3O_5 grains. The metallic iron are present as globules inside the silicate grains.

The M_3O_5 phase is a pseudobrookite, and requires further description.

2.3.2 Pseudobrookite

The ternary phase diagram FeO-Fe_2O_3-TiO_2 is shown in Figure 2.4 [5]. There is a considerably large amount of confusion regarding the term *pseudobrookite*. This part will provide a clarification of the term in general, and specify what the term means in the context of this thesis.

The pseudobrookite structure includes structures on the form M_3O_5 containing mainly Ti, Fe, O, and appreciable concentrations of other elements (Mg, Cr, Al, V, Mn, Ca, Zr, etc). Minerals with this structure contain varying proportions of Fe^{2+}, Fe^{3+}, Ti^{3+} and Ti^{4+} [21].

The pseudobrookite *mineral* (not to be confused with the pseudobrookite *structure*) has the ideal formula Fe_2TiO_5. It is limited by the compounds $FeTi_2O_5$ (ferropseudobrookite) and $FeMg_{0.5}Ti_{1.5}O_5$ as defined in [6]. The pseudobrookite mineral can be found naturally and often contain considerable amounts of Mg, Mn, Al and Cr.

Another mineral with the pseudobrookite structure is Armalcolite. Armalcolite is named after the crew of the Apollo 11 moon landing (Neil A. **Arm**strong, Edwin E. **Al**drin and Michael **Col**lins) because it is found in appreciable amounts on the moon [22]. Armalcolite has the ideal formula $Fe_{0.5}Mg_{0.5}Ti_2O_5$, and is limited by the following compounds: $MgTi_2O_5$, $FeTi_2O_5$, $FeMg_{0.5}Ti_{1.5}O_5$ and $Mg_{0.5}Ti_{2.5}O_5$.

The third main mineral with the pseudobrookite structure is Anosovite. It has the ideal formula Ti_3O_5. Anosovites usually have high Al contents, small Fe contents, and traces of Mg, Mn, Ca, Cr and V.

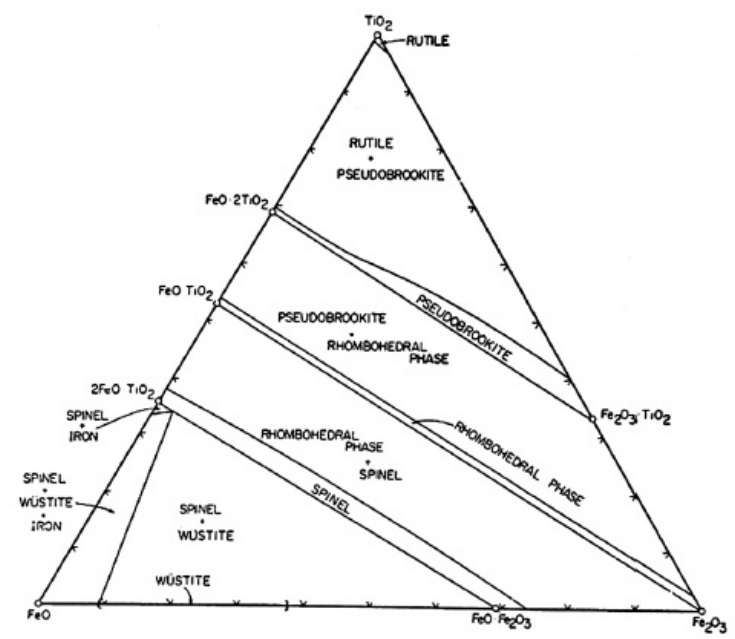

Figure 2.4: The FeO-Fe_2O_3-TiO_2 ternary phase diagram [5]

Structure	Space group	Density [g/cm^3]	Unit cell parameters [Å]
Rutile	*$P4_2$/mnm*	4.25	a = b = 4.593 c = 2.959
Anatase	*$I4_1$/amd*	3.89	a = b = 3.785 c = 9.513
Brookite	*Pbca*	4.12	a = 5.455 b = 9.181 c = 5.142

Table 2.2: The lattice parameters of the three TiO_2 polymorphs rutile, anatase and brookite [23]

The definitions and boundaries presented here are summarized in Figure 2.5. The series from pseudobrookite to anosovite is shown along the vertical axis on the left, with the amount of Mg increasing from left to right. The elements Mn and Ca are plotted as Mg. The diagonal lines in the diagram specify the amount of $(Al,Cr,V)_2(Ti,Zr)O_5$ in previously studied samples. The length of the line is proportional to the amount $(Al,Cr,V)_2(Ti,Zr)O_5$ present.

The term *pseudobrookite* will be used further in this thesis for phases corresponding to the pseudobrookite field shown in Figure 2.5. From the description given it is evident that this phase will be likely to contain Mg, Mn, Al and/or Cr in addition to Fe, Ti and O. This phase has an orthorhombic structure of O^{2-} anions with the cations in octahedral positions. The unit-cell parameters are approximated to $a = 9.743$, $b = 10.024$ and $c = 3.738$ Å.

2.3.3 TiO_2

TiO_2 exists in a large number of polymorphs. These include rutile, anatase, brookite, columbite, baddeleyite and cotunnite [23]. The latter three are high-pressure phases and are not relevant to this thesis. Therefore, the three variations of TiO_2 to be reviewed are rutile, anatase and brookite.

Of these three, only rutile is thermodynamically stable. The transformation brookite $\rightarrow$ rutile occurs in the range $500\,^{\circ}\mathrm{C}$ to $700\,^{\circ}\mathrm{C}$ [24], and the transformation anatase $\rightarrow$ rutile occurs in the range $600\,^{\circ}\mathrm{C}$ to $1100\,^{\circ}\mathrm{C}$ [25].

The three TiO_2 polymorph structures differ from each other in the following way. Rutile has a tetragonal structure with the space group *$I4_2$/mnm*, made by chains of TiO_6 octahedral sites sharing a vertex along the c-axis. Anatase has a tetragonal structure with the space group *$I4_1$/amd*, made up from distorted TiO_6 octahedral sites sharing four corners. Lastly, brookite has an octahedral structure with the space group *Pbca*, made up by distorted TiO_6 octahedra sharing three edges. The structures of the TiO_2 polymorphs are shown in Figure 2.6, while the lattice parameters are given in Table 2.2.

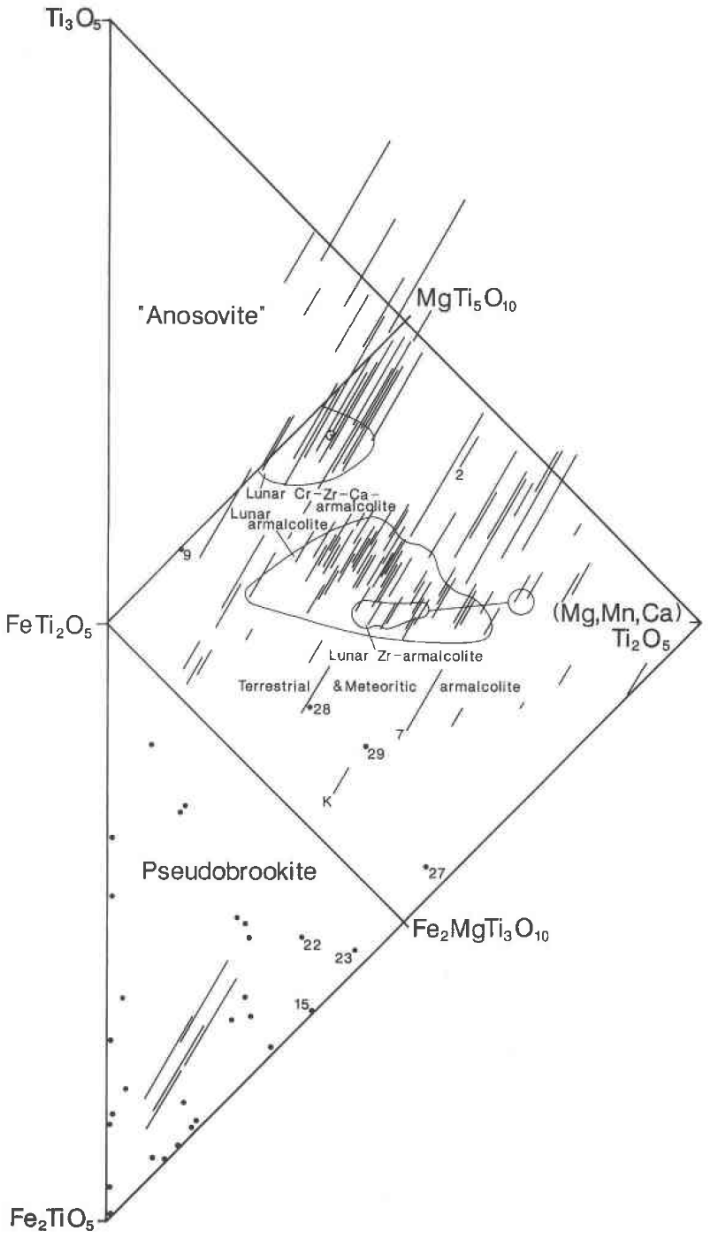

Figure 2.5: The pseudobrookite structures [6]

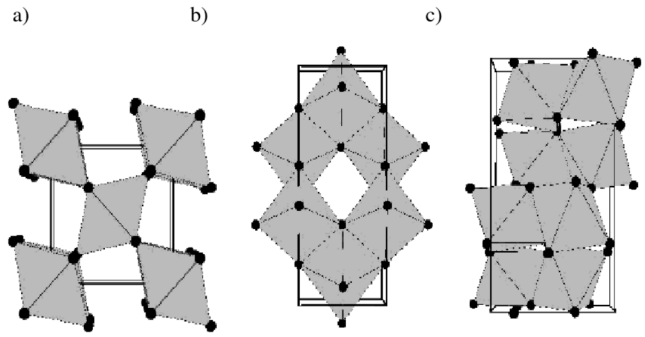

[a] Structure of rutile, along plane *ab*.
[b] Structure of anatase, along plane *ac*.
[c] Structure of brookite, along plane *ab*.

Figure 2.6: The lattice structures of the three TiO_2 polymorphs rutile, anatase and brookite [23]

Chapter 3

Literature Review

3.1 XRD analysis of Ti slags

XRD analysis of titanium slags with emphasis on rutile was done by *A. Przepiera* and *M. Jablonski* in 2003 [7]. In this work, a titanium slag from QIT with the composition Ti-47.4%, Fe-8.1%, Mg-3%, Si-2.1%, Al-1.9% was used. The work analyzed the effect of grain size of the crushed samples on phase transformation rates using thermogravimetry and x-ray diffraction.

Spectrographs of the original slag and slag calcined at 900 °C are shown in Figure 3.1. The original slag has a diffractogram closest to that of the pure synthetic phase magnesium titanate ($MgTi_2O_5$) and contains a small amount of rutile phase. The calcined slag has a diffractogram showing a more pronounced rutile pattern.

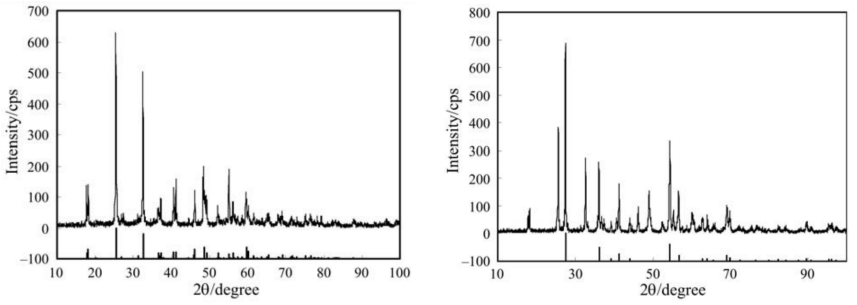

(a) $MgTi_2O_5$ **(b)** Rutile

Figure 3.1: XRD spectras of $MgTi_2O_5$ and rutile phases [7]

Spectrographs taken during heating is shown in Figure 3.2. The phase change from magnesium titanate to ferric pseudobrookite (Fe_2TiO_5) and rutile is seen at increasing temperature. The most easily distinguishable difference is the increasing prevalence of the

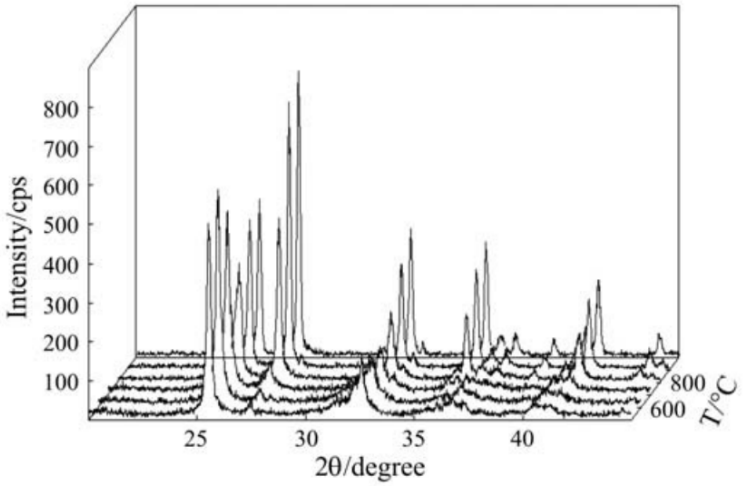

Figure 3.2: XRD spectras of Ti slag during heating [7]

rutile peak at $2\theta = 27°$ with increasing temperature.

3.2 Composition of Sorelslag

An analysis featuring XRD, chemical analysis and SEM micrographs was done by *I. Toromanoff* and *F. Habashi* in 1984 [8]. This work also analyzed a slag from the Canadian company QIT. The chemical analysis from the slag is given in Table 3.1. The residue in the table was obtained by baking the slag with H_2SO_4 at 200 °C and then leaching with water. The chemical analysis indicates that titanium is present in both the trivalent and tetravalent states, while iron is mainly in its ferrous state, with little in its metallic state.

	Slag (%)	Residue (%)
TiO_2 (total)	71.5	30.2
Ti_2O_3 (expressed as TiO_2)	9.4	
TiO_2 (insoluble in H_2SO_4)	1.87	
Fe (total)	9.7	4.0
Fe (metallic)	0.8	
Fe_2O_3	0.0	
Al_2O_3	4.5	11.95
SiO_2	4.2	39.95
CaO	0.7	4.95
MgO	5.1	
MnO	0.2	
V_2O_5	0.57	
Cr_2O_5	0.19	
P_2O_5	0.03	
C	0.02	
S	0.06	

Table 3.1: Chemical analysis of a QIT slag and the residue left after leaching with H_2SO_4 [8]

The XRD analysis showed a close match to the mineral Armalcolite represented as $Fe_{0.5}Mg_{0.5}Ti_2O_5$. The analysis also detected a trace of rutile.

The light microscope images and SEM images show the following phases: (1) a light grey phase composed of titanium, iron, and magnesium; (2) a dark grey phase composed of silicon, calcium, iron, titanium, aluminium, potassium, and manganese; (3) small globules of metallic iron; (4) large globes of metallic iron. The phases are shown in Figure 3.3.

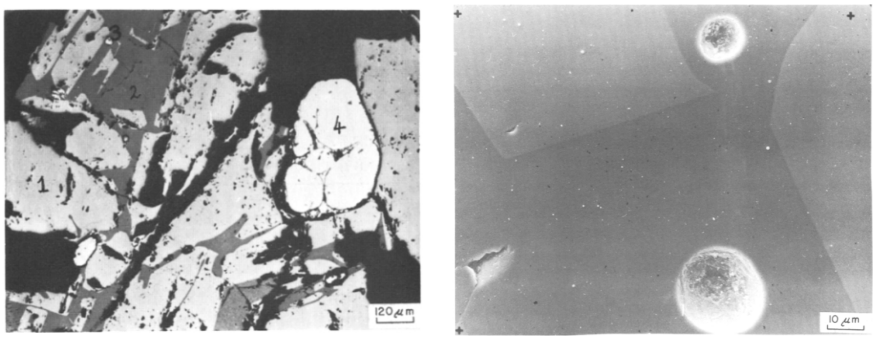

(a) Light micrograph **(b)** SEM micrograph

Figure 3.3: Micrographs of phases present in a QIT slag. The SEM micrograph shows the small iron globules incorporated in the titanium and silicate phases [8]

The small iron globules seen in Figure 3.3b are probably from a different origin than the large globules. They seem to be nucleated during cooling through the reaction given in Equation 3.1. This corresponds to the reaction given in Equation 3.2. This reaction has a

standard free-energy change of $-17\,\mathrm{kcal\,mol^{-1}}$ at $1000\,^{\circ}\mathrm{C}$, thus making it thermodynamically feasible.

It is believed that the difference in coefficient of expansion of the metallic iron and the slag makes the slag deprecate and crack while cooling.

$$2Ti^{3+} + F^{2+} \rightarrow 2Ti^{4+} + Fe^{0} \tag{3.1}$$

$$Ti_2O_3 + FeO \rightarrow 2TiO_2 + Fe^{0} \tag{3.2}$$

3.3 Laser Flash Analysis

There is a lack of thermal analysis using the laser flash method on titanium slags. This part will then instead review work done on various ores.

3.3.1 Manganese ores

An extensive thermal study on manganese ores was conducted by *M. Ksiazek* in 2012 [9]. This work conducts analysis on various manganese ores, using both solid and powder samples.

The types of thermal experiments conducted on the solid and powder samples are shown in Table 3.2. All experiments in the table is done as a function of temperature.

	Solid	Powder
Porosity	X	
Mass loss	X	
Thermal expansion	X	X
Thermal conductivity	X	X
Specific heat	X	X

Table 3.2: Thermal experiments done in [9]

The thermal expansion tests were conducted in atmospheres of air and N_2. The powder samples were made with particle sizes of $90\,\mu\mathrm{m}$-$180\,\mu\mathrm{m}$, and $<63\,\mu\mathrm{m}$. The tests were conducted from room temperature to $1000\,^{\circ}\mathrm{C}$. Some of the powder samples were initially sintered at $1100\,^{\circ}\mathrm{C}$ for $30\,\mathrm{min}$. The results from some of the thermal expansion tests are shown in Figure 3.4.

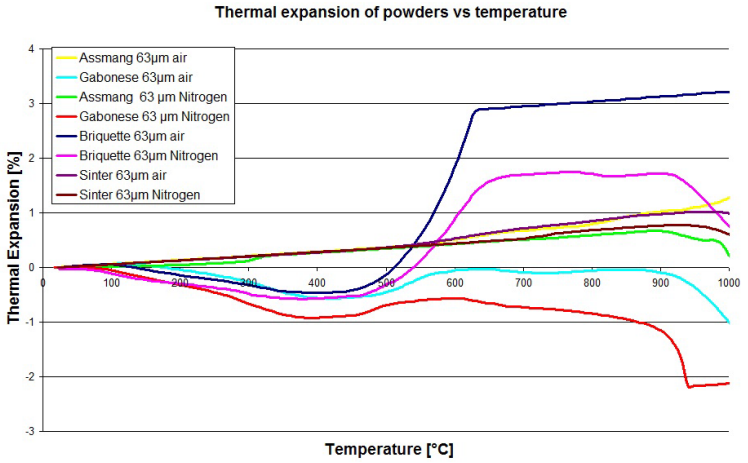

Figure 3.4: Thermal expansion results from [9]

The sintered samples steadily increase in length for the entire duration of the experiment, while some of the other samples tend to shrink until $450\,^{\circ}\mathrm{C}$ before expanding. In most cases, the thermal expansion is not greater than $\pm 2\%$ from room temperature to $1000\,^{\circ}\mathrm{C}$.

The thermal conductivity experiments were conducted on the same sample types as the expansion tests, and also conducted from room temperature to $1000\,^{\circ}\mathrm{C}$. All conductivity experiments were done in an N_2 atmosphere. The *LFA 457 MicroFlash* was used for both the conductivity and following specific heat experiments. Results from one of the ore types is shown in Figure 3.5.

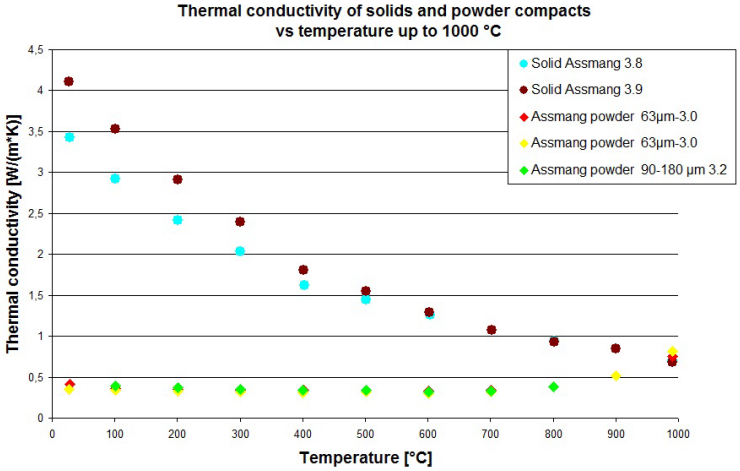

Figure 3.5: Thermal conductivity results from [9]

From this and other results in the same work, it is seen that the particle size of the powdered pellets does not affect the conductivity significantly. It is also readily seen that the conductivity of the powdered samples are far lower than that of the solid samples. Because the conductivity of the solid samples decrease heavily with increasing temperature, the conductivity of the solid and powdered samples are closest at high temperatures. All the powder samples analysed had a very slight increase in conductivity at higher temperatures. The conductivity for the powdered samples are for the most part measured to be between $0.2\,\mathrm{W\,m^{-1}\,K}$ and $1.0\,\mathrm{W\,m^{-1}\,K}$.

Specific heat as function temperature is calculated from the same experimental runs as the conductivity. The results for the same samples as in Figure 3.5 is shown in Figure 3.6.

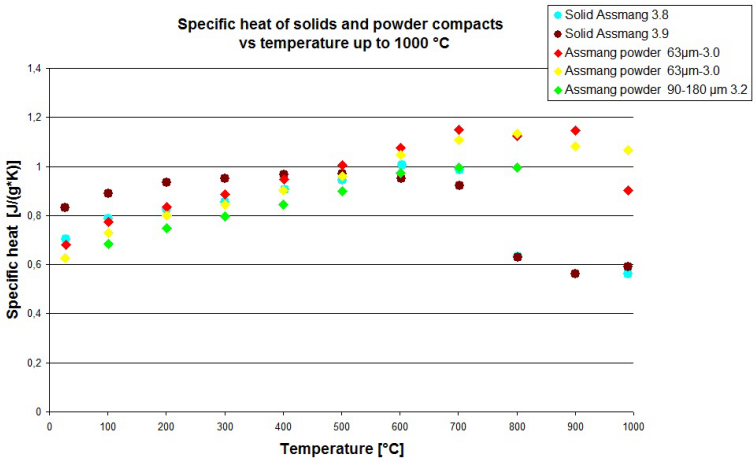

Figure 3.6: Specific heat results from [9]

The powder samples shows a steady increase in heat capacity with increasing temperature, but show a slight decrease towards $1000\,^{\circ}\mathrm{C}$. The specific heat for the solid samples, however, show a clear decline after $700\,^{\circ}\mathrm{C}$. All samples are mostly confined in the interval $0.6\,\mathrm{J\,g^{-1}\,K}$ to $1.2\,\mathrm{J\,g^{-1}\,K}$ for all measured temperatures.

3.3.2 Iron ores

A study on thermal conductivity of iron ores was conducted by *T. Akiyama et al.* in 1992. [10]. Dense pure iron ores as well as fired and non-fired pellets were analyzed. The pure iron ore samples were hot pressed at $1173\,\mathrm{K}$ with a force of $150\,\mathrm{MPa}$ for $7200\,\mathrm{s}$ in a pure argon atmosphere. The samples were pressed from powders of average particle size $1\,\mu\mathrm{m}$.

The porosity of the hot pressed samples were measured to be less than 0.1%. The expansion with respect to temperature was measured but not given in the article.

Samples of $1\,\mathrm{cm}$ in diameter and $1\,\mathrm{cm}$ to $1.5\,\mathrm{cm}$ in thickness were analyzed in a laser flash apparatus in a vacuum between room temperature and $1553\,\mathrm{K}$. The thermal conductivity results from the hot pressed samples are shown in Figure 3.7. It is readily seen

that the conductivity of the samples vary highly with composition. Within the temperature interval, readings are found between $4\,\mathrm{W\,m^{-1}\,K}$ and $60\,\mathrm{W\,m^{-1}\,K}$.

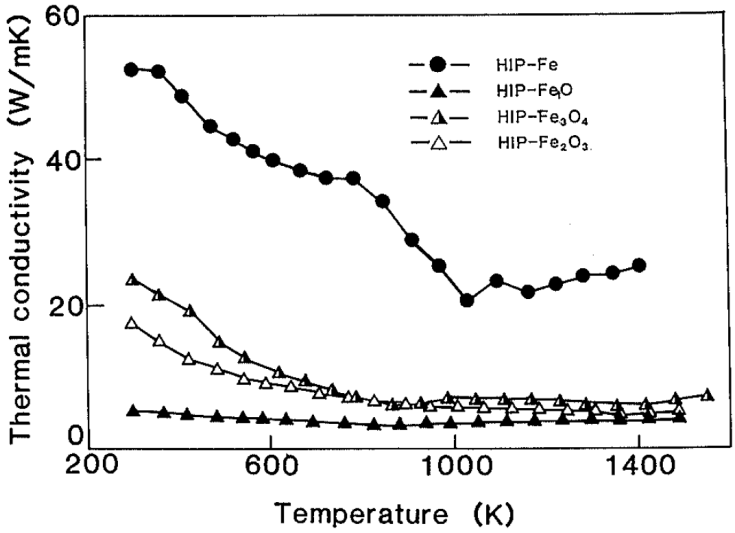

Figure 3.7: Thermal conductivity results from [10]

Non-fired pellets were made from iron ore powders mixed with 7 mass% cement, and cured in room temperature for 10 days. Fired pellets and sintered samples was also analyzed. A collection of results for the thermal diffusivity of the different sample types is shown in Figure 3.8. Thermal diffusivity is thermal conductivity divided by density and specific heat, as seen in Equation 2.5 in Section 2.1.1

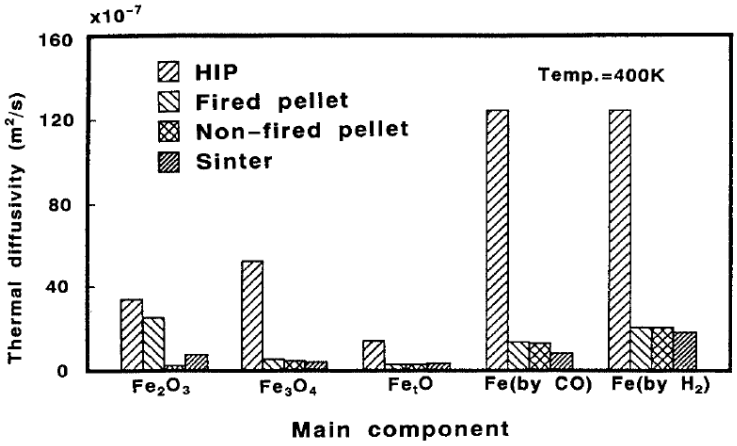

Figure 3.8: Thermal diffusivity results from [10]

It is evident that the hot pressed samples exhibit a much greater thermal diffusivity (and thus conductivity) than the three other types of samples made from the same material.

Chapter 4

Method

4.1 Sample gathering

Samples were gathered from the industrial plant *Tizir Titanium & Iron* in Tyssedal, Norway. Sample collection was done on two different occasions: Firstly between July 21st and July 23rd 2015 by the author, and secondly between January 25th and January 27th 2016 by the staff in Tyssedal. As previously mentioned, the plant in Tyssedal changed the end product from sulphate grade slag to chloride grade slag between these two occasions. The two sets of samples therefore exhibit differences in chemical contents.

The same procedure was carried out during both sample collections. The procedure was as follows:

The tapping and preliminary cooling of the slag was carried out as explained in Section 1.2.3. After the initial 3 hours cooling with water spray, one of the slag cakes was removed from the usual process and set aside to cool in air for 7 days. One other slag cake followed the usual cooling process of water sprays for 3 days. From each of the two slag cakes, samples were collected at three sites: the top, center and bottom of the cakes. The samples collected from slag cakes are shown schematically in Figure 4.1.

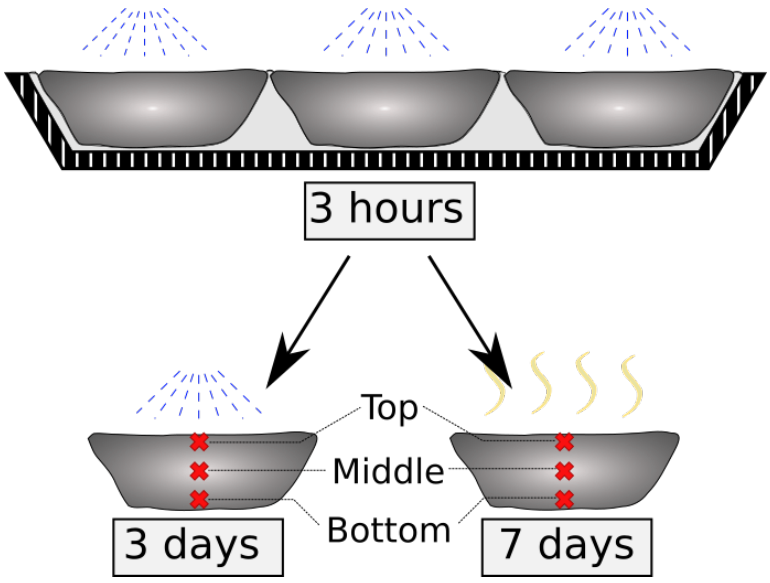

Figure 4.1: Cooling of slag cakes at Tizir Titanium & Iron

The cooling rate of the slag cake is highest at the top because of water sprays, and easy access to air for the non-sprayed cake. The center of the cake will exhibit the slowest cooling rate, while the bottom will be somewhere in the middle ground between the two.

A sample was also collected directly from the tapping stream. This was done by dipping a steel rod into the tapping stream. The slag solidified on the rod experienced a very fast cooling compared to all the other samples.

An overview of all the samples collected industrially is shown in Table 4.1. The sample set containing the sulphate-grade samples have been analyzed in a previous work, and will be referenced throughout [26]. The chemical analysis performed on the sulphate and chloride samples are shown in Tables 4.2-4.3 and 4.4-4.5, respectively.

		Sulphate grade	Chloride grade
Air cooling	Top	*S-At*	*C-At*
	Center	*S-Ac*	*C-Ac*
	Bottom	*S-Ab*	*C-Ab*
Water cooling	Top	S-Wt	C-Wt
	Center	*S-Wc*	*C-Wc*
	Bottom	*S-Wb*	*C-Wb*
Tapping stream		*S-T*	*C-T*

Table 4.1: Names applied to all the samples throughout this thesis

	S-S	S-Wt	S-Wb	S-Wc	S-At	S-Ab	S-Ac
$\%TiO_2$	79,18	79,45	76,72	76,82	78,11	76,29	77,54
$\%FeO$	8,56	9,53	9,95	10,19	9,94	10,40	9,58
$\%MnO$	0,56	0,54	0,59	0,60	0,56	0,59	0,54
$\%CaO$	0,58	0,55	0,64	0,62	0,63	0,70	0,62
$\%MgO$	5,99	5,84	5,87	5,89	5,80	5,87	5,81
$\%SiO_2$	4,75	4,32	5,00	4,86	4,48	4,80	4,37
$\%Cr_2O_3$	0,131	0,129	0,132	0,139	0,140	0,140	0,137
$\%V_2O_5$	0,314	0,318	0,305	0,304	0,312	0,310	0,313
$\%Al_2O_3$	1,81	1,75	1,90	1,83	1,74	1,77	1,73
$\%Nb$	0,021	0,015	0,017	0,016	0,020	0,020	0,021
$\%Zn$	0,0021	0,0010	0,0010	0,0003	0,0030	0,0040	0,0003
$\%ZrO_2$	0,067	0,064	0,070	0,069	0,070	0,068	0,065
$\%Ba$	0,0107	0,0114	0,0112	0,0105	0,0106	0,0111	0,0126
$\%C$	0,011	0,011	0,011	0,011	0,011	0,011	0,011
$\%S$	0,004	0,000	0,000	0,003	0,005	0,002	0,001

Table 4.2: Elemental analysis of the sulphate samples gathered in July 2015 at the industrial plant Tizir Titanium & Iron in Tyssedal, Norway [26]

	S-S	S-Wt	S-Wb	S-Wc	S-At	S-Ab	S-Ac
$\%Fe$ Metallic	0,3	1,2	0,7	0,9	0,4	1,2	0,7
$\%FeO$	8,6	9,5	10,0	10,2	9,9	10,4	9,6
$\%TiO_2$ insoluble	0,9	1,10	3,60	0,01	0,70	0,07	0,20
$\%Ti_2O_3$ as TiO_2	23,3	18,8	12,4	17,8	15,5	9,3	4,2

Table 4.3: Wet chemical analysis of the sulphate samples gathered in July 2015 at the industrial plant Tizir Titanium & Iron in Tyssedal, Norway [26]

	C-S	C-Wt	C-Wb	C-Wc	C-At	C-Ab	C-Ac
$\%TiO_2$	87,27	88,13	86,79	87,56	85,82	85,35	87,48
$\%FeO$	9,03	8,38	9,27	8,81	8,95	9,24	8,77
$\%MnO$	1,58	1,34	1,56	1,44	1,44	1,50	1,50
$\%CaO$	0,10	0,07	0,09	0,08	0,09	0,08	0,09
$\%MgO$	1,07	1,95	0,99	1,09	1,12	0,99	1,02
$\%SiO_2$	1,82	1,42	1,74	1,52	1,69	1,57	1,77
$\%Cr_2O_3$	0,218	0,206	0,226	0,218	0,217	0,225	0,216
$\%V_2O_5$	0,353	0,360	0,350	0,255	0,345	0,344	0,345
$\%Al_2O_3$	1,65	1,56	1,61	1,59	1,55	1,54	1,62
$\%Nb$	0,089	0,076	0,086	0,078	0,082	0,081	0,090
$\%Zn$	-	-	-	-	-	-	-
$\%ZrO_2$	0,269	0,226	0,253	0,236	0,242	0,244	0,253
$\%Ba$	0,0084	0,0078	0,0073	0,0071	0,0081	0,0071	0,0081
$\%C$	0,010	0,009	0,009	0,009	0,010	0,009	0,009
$\%S$	0,005	0,005	0,002	0,001	-	-	-

Table 4.4: Elemental analysis of the chloride samples gathered in January 2016 at the industrial plant Tizir Titanium & Iron in Tyssedal, Norway

	C-S	C-Wt	C-Wb	C-Wc	C-At	C-Ab	C-Ac
$\%Fe$ Metallic	0,3	0,2	1,1	0,14	0,19	0,44	0,1
$\%FeO$	9,03	8,38	9,27	8,81	8,95	9,24	8,77
$\%TiO_2$ insoluble	2,5	5,9	-	6,2	-	-	6,1
$\%Ti_2O_3$ as TiO_2	30,1	20,6	20,4	23,5	1,5	3,5	29,6

Table 4.5: Wet chemical analysis of the sulphate samples gathered in January 2016 at the industrial plant Tizir Titanium & Iron in Tyssedal, Norway

4.2 Melting experiments

Another set of samples was made by the author be re-melting industrially collected samples in a small scale induction furnace. The samples made this way were cooled in a more controlled environment than in the industrial process. The temperature of the cooling slag was measured to obtain exact knowledge of the cooling rates in question.

The material used for the melting experiments was a crushed mix of the sulphate grade water cooled samples. In each batch, $1\,\mathrm{kg}$ of the slag was collected in a carbon crucible. The carbon crucible was $40\,\mathrm{cm}$ tall, and had inner and outer diameters of 12 and $15\,\mathrm{cm}$, respectively. A carbon tube was inserted down the middle of the crucible to hold a type C thermocouple. The setup is shown in Figure 4.2.

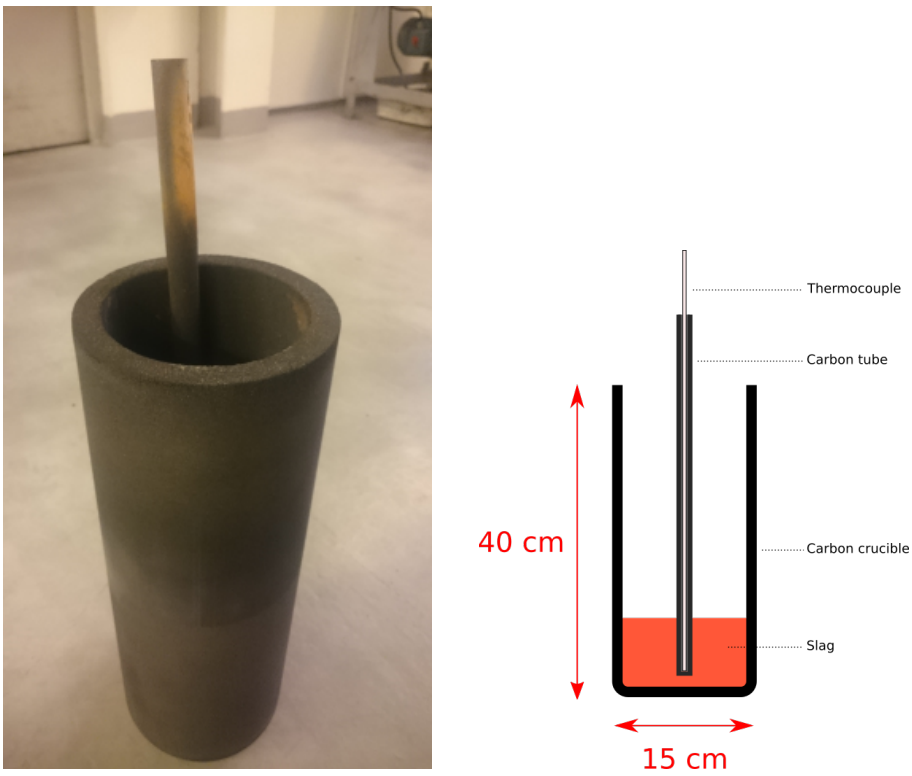

(a) Picture **(b)** Sketch

Figure 4.2: Crucible used for melting experiments. Contains $1\,\mathrm{kg}$ of crushed slag

The crucible was heated using an *Inductotherm IF75* induction furnace with a power supply of maximum $75\,\mathrm{kW}$. The furnace setup with the crucible is shown in Figure 4.3.

Figure 4.3: IF75 furnace used in the melting experiments

Three similar experiments was conducted using this furnace. In all three cases, the crucible was heated at a constant power of $30\,\mathrm{kW}$. This results in a heating time from room temperature to $1650\,^{\circ}\mathrm{C}$ of about $25\,\mathrm{min}$. After completely melting the slag, the samples were cooled and their temperature drop measured. To obtain different cooling rates for the three experiments, the cooling was handled as follows:

- **Fast**: The crucible was removed from the furnace to receive a fast cooling rate.
- **Medium**: The crucible was left in the furnace with the power switched off. The furnace lining acts as an insulator, giving the sample a slower cooling rate.
- **Slow**: The crucible was left in the furnace. The power on the furnace was carefully controlled to give the sample a slow cooling rate.

The cooling rates obtained for the three samples are shown in Figure 4.4. The temperature history of the sample *Slow* was done by keeping the induction power at $5\,\mathrm{kW}$ for $30\,\mathrm{min}$, then $4\,\mathrm{kW}$ for $50\,\mathrm{min}$, $3\,\mathrm{kW}$ for $60\,\mathrm{min}$, and finally turned off for the remaining duration of the experiment.

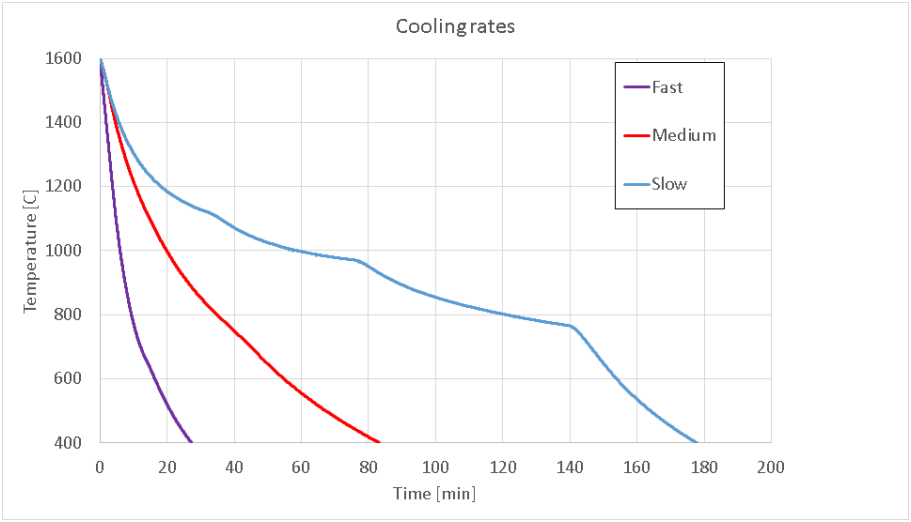

Figure 4.4: Cooling rates obtained for the three samples prepared in the IF 75 induction furnace

4.3 Sample preparation

Both samples which were collected industrially and made in the induction furnace were prepared for analysis as follows.

Samples to be used for SEM imaging and EDS analysis was cut to size and mounted in an epoxy resin. After grinding and polishing the surface to be analyzed, the samples were wrapped in aluminium foil. This is done to conduct electrons from the sample surface to the sample holder in the electron microscope. The finished sample is shown in Figure 4.7a.

To prepare powder samples, the slag was first crushed in a steel mortar, and then crushed in a *Siebtechnik* crushing machine. The machine consists of several steel cylinders, crushing the slag to a fine powder with a rotation of $960\,\mathrm{rpm}$. It is shown in Figure 4.5. The powdered slag was then sifted to ensure a particle size of $<71\,\mu\mathrm{m}$. The powder after sifting is shown in Figure 4.7b.

(a) Picture **(b)** Sketch

Figure 4.5: Crushing machine used for crushing the slag to a fine powder. Sketch shows the steel cylinders used for crushing

Samples for thermal expansion tests and Laser Flash analysis both require pressing the powdered slag to cylindrical pellets. The press used is shown in Figure 4.6. The samples used to measure thermal expansion were pressed to a diameter of $5\,\mathrm{mm}$, and an approximate length of $10\,\mathrm{mm}$. The samples for Laser Flash analysis were pressed to a diameter of $12.7\,\mathrm{mm}$, and an approximate length of $2\,\mathrm{mm}$. The samples for use in thermal expansion and Laser Flash analysis are shown in Figures 4.7c and 4.7d, respectively.

For both types of pressed samples, a pressure of $80\,\mathrm{MPa}$ was applied. As the pressing tool is operated by controlling force, this pressure results in a force of $1.57\,\mathrm{kN}$ for the $5\,\mathrm{mm}$ samples, and a force of $10.1\,\mathrm{kN}$ for the $12.7\,\mathrm{mm}$ samples.

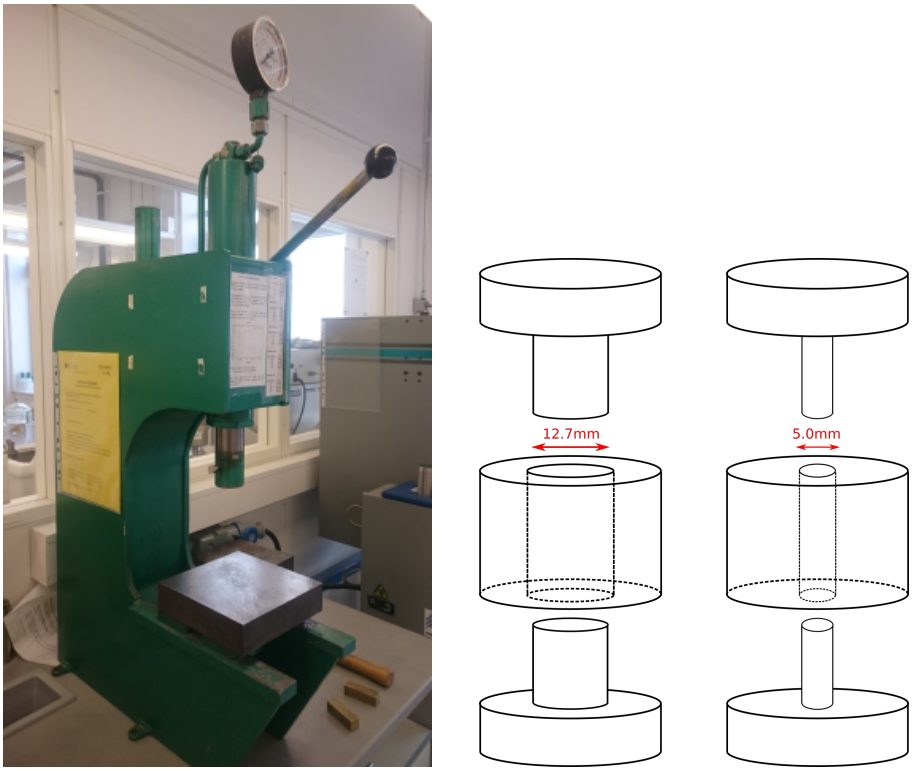

(a) Picture **(b)** Sketch

Figure 4.6: Cylindrical press used to make pellets. Sketch shows the pressing containers used.

4.4 Analysis methods

4.4.1 SEM imaging and EDS analysis

The samples, as previously shown in Figure 4.7a, were studied using a *FESEM Zeiss Ultra 55*. The images were taken with parameters as follows. The EDS analysis was done under the same conditions.

- WD: 10 mm
- EHT: 15 kV
- High current mode
- Magnification 100x / 500x

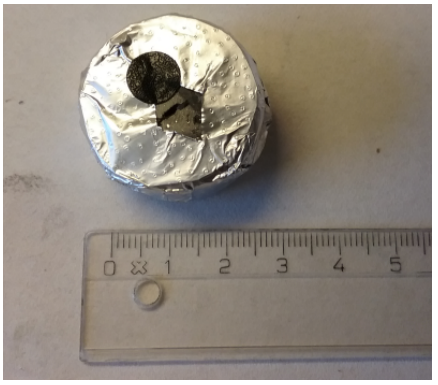

(a) SEM sample

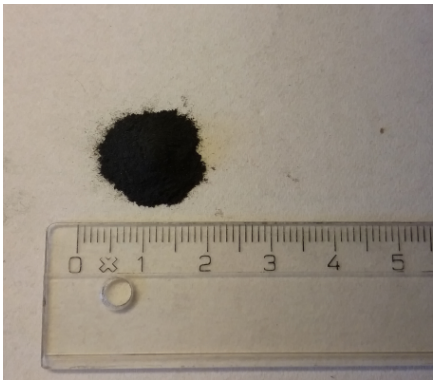

(b) Powder sample $<71\,\mu\mathrm{m}$

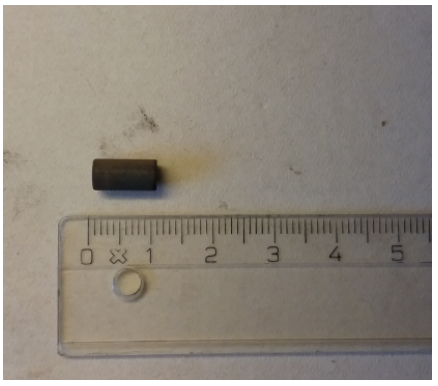

(c) Rod for thermal expansion analysis

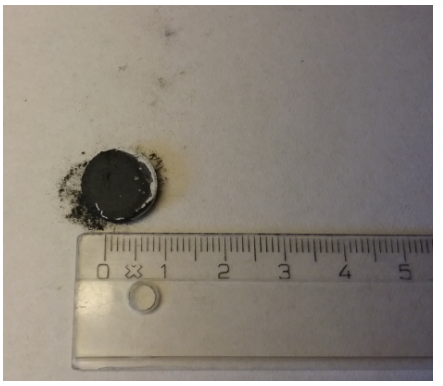

(d) Pellet for Laser Flash analysis

Figure 4.7: The four types of samples prepared for analysis.

4.4.2 XRD

The diffraction analysis was done using a $BrukerD8 - Focus$ with a copper K_α X-ray tube, using a $1\,\mathrm{mm}$ slit. The analysis parameters were as follows:

- 2θ range: $10°$ - $60°$
- 2θ step length: $0.025°$
- Step measure time: $2\,\mathrm{s}$
- Total measure time: $66\,\mathrm{min}$

The powders analyzed were all of particle size $<71\,\mu\mathrm{m}$.

4.4.3 Thermal expansion

Apparatus

Thermal expansion experiments were conducted using a *Netzsch 402E* dilatometer. The apparatus is shown in Figure 4.8.

The sample is mounted horizontally in a sample holder located inside a furnace. Alumina end plates are placed at both ends of the sample for stability. As the sample is heated to the desired temperatures, the displacement transducer records the expansion of the sample carried through the push rod. Because the transducer shown in the figure cannot be subject to the high temperatures inside the furnace chamber, the alumina push rod has to be used. As the push rod expands along with the sample during the experiment, this has to be accounted for during the result analysis.

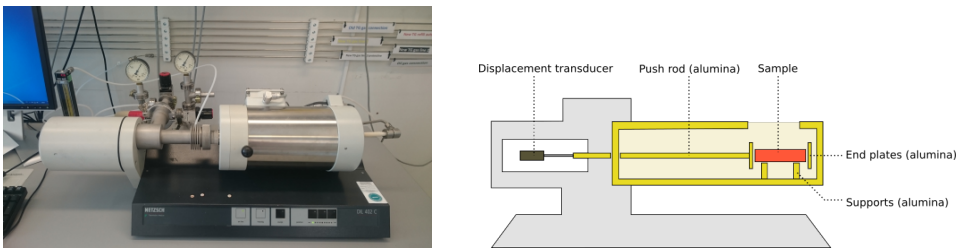

(a) Picture **(b)** Sketch

Figure 4.8: Dilatometer apparatus *Netzsch 402E*

The easiest way to account for the expansion of the push rod and the sample holder, is to first do a reference measurement on a rod of known expansion properties. The reference measurement has to be done under the exact same conditions and with the same experimental parameters. An alumina rod of $5\,\mathrm{mm}$ in diameter and $20\,\mathrm{mm}$ long was used as a reference.

Method

The measurements were done in a N_2 atmosphere with a flow rate of $30\,\mathrm{ml\,min^{-1}}$. The temperature scheme was set from $28\,^{\circ}\mathrm{C}$ to $800\,^{\circ}\mathrm{C}$ with a constant temperature increase of $2\,^{\circ}\mathrm{C\,min^{-1}}$. The temperature decrease was set from $800\,^{\circ}\mathrm{C}$ to $28\,^{\circ}\mathrm{C}$ with a constant temperature reduction of $2\,^{\circ}\mathrm{C\,min^{-1}}$.

The analysis was run with the alumina rod as a reference.

4.4.4 Laser Flash

Apparatus

Experiments were conducted using the instrument *LFA 457 MicroFlash* shown in Figure 4.9.

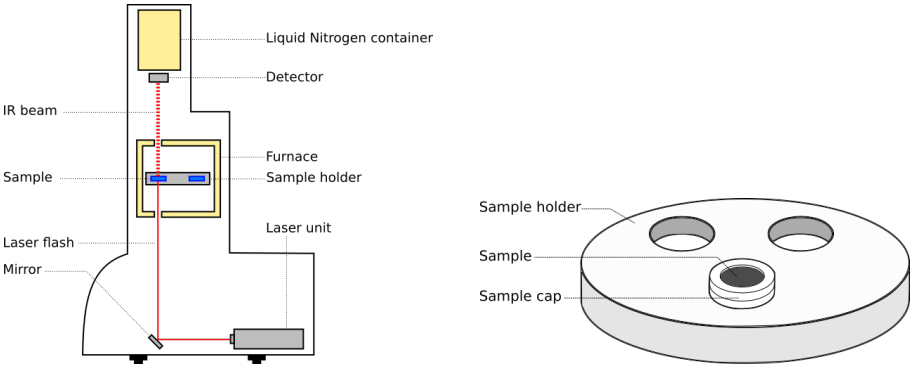

(a) LFA apparatus **(b)** LFA sample holder

Figure 4.9: Sketch of the laser flash apparatus MicroFlash 457 and the sample holder used

Method

Samples were crushed, sifted and pressed as explained in Section 4.3. The samples were coated with a carbon spray on both sides prior to mounting in the sample holder. Each analysis was run with two slag samples and one reference sample.

The analysis was conducted in a N_2 atmosphere with a flow rate of $100\,\mathrm{ml/\,min}$. To determine the analysis parameters, test flashes are first done at room temperate. The pulse strength and acquisition duration is manipulated until the temperature reading is within a satisfactory threshold. When satisfactory parameters are found, the analysis is started using the wanted temperature scheme.

- Temperature range: $25\,^{\circ}\mathrm{C}$-$800\,^{\circ}\mathrm{C}$
- Temperature interval: $100\,^{\circ}\mathrm{C}$
- Data acquisition duration: $35\,000\,\mathrm{ms}$
- Laser pulse strength: $1826\,\mathrm{V}$

Chapter 5

Results

5.1 SEM images

The SEM images taken as described in Section 4.4.1 are shown in Figures 5.2 through 5.11. Figure 5.1 shows the phases occurring in the samples.

SEM images of the *sulphate-grade* sample set it shown as reference in Figures 5.12 through 5.15.

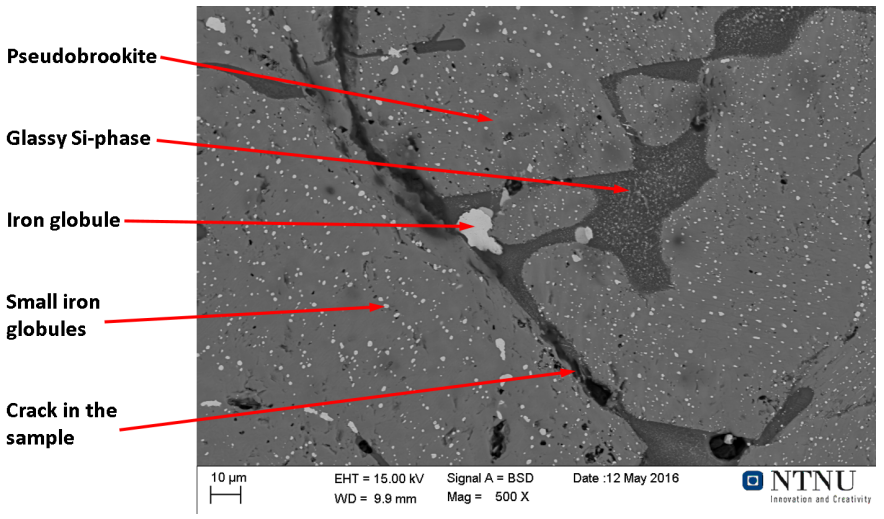

Figure 5.1: SEM image of the sample C-Ab at 500x magnification. The most common phases are as marked. The only phase occurring in the other samples and not in this one, is the rutile phase.

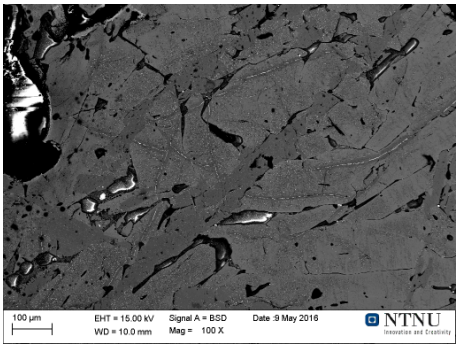

(a) 100x magnification **(b)** 500x magnification

Figure 5.2: SEM images of sample C-At

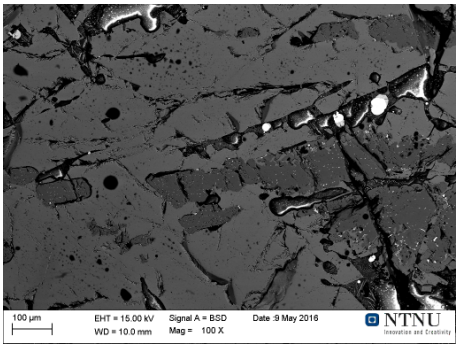

(a) 100x magnification **(b)** 500x magnification

Figure 5.3: SEM images of sample C-Ac

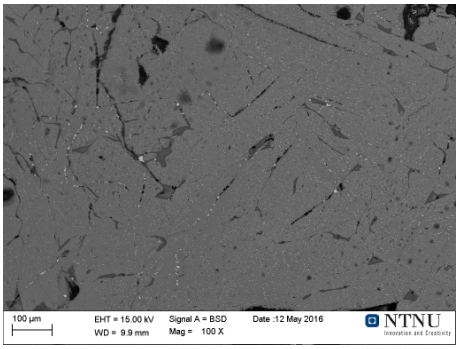

(a) 100x magnification **(b)** 500x magnification

Figure 5.4: SEM images of sample C-Ab

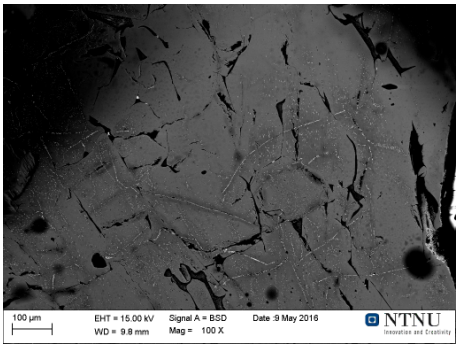

(a) 100x magnification **(b)** 500x magnification

Figure 5.5: SEM images of sample C-Wt

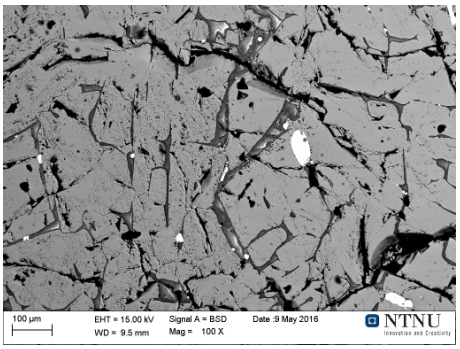

(a) 100x magnification **(b)** 500x magnification

Figure 5.6: SEM images of sample C-Wc

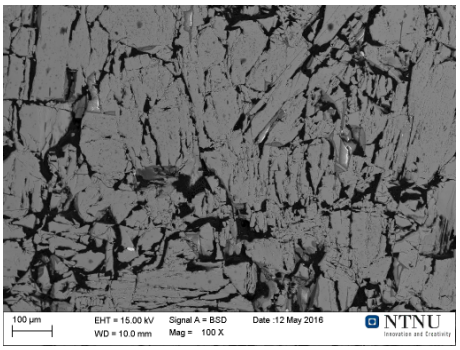

(a) 100x magnification **(b)** 500x magnification

Figure 5.7: SEM images of sample C-Wb

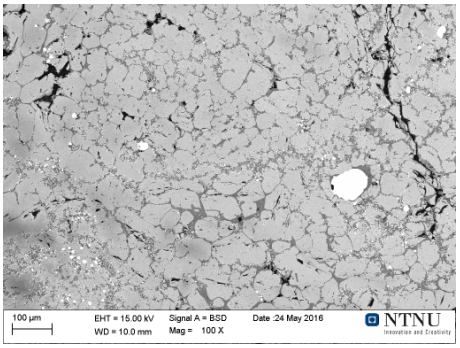

(a) 100x magnification **(b)** 500x magnification

Figure 5.8: SEM images of sample IF-slow

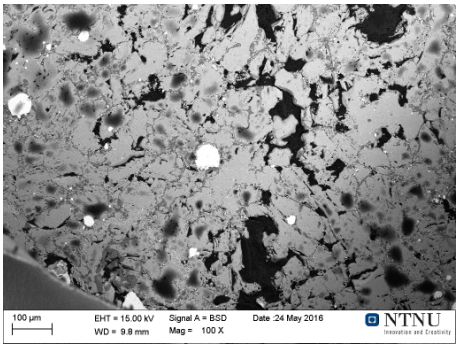

(a) 100x magnification **(b)** 500x magnification

Figure 5.9: SEM images of sample IF-medium

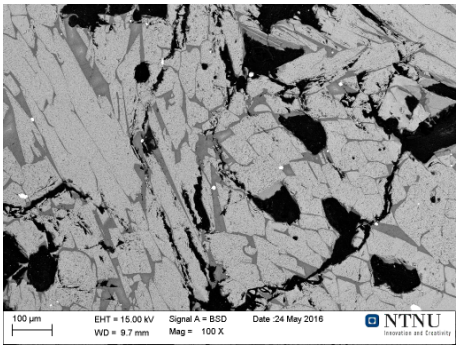

(a) 100x magnification **(b)** 500x magnification

Figure 5.10: SEM images of sample IF-fast

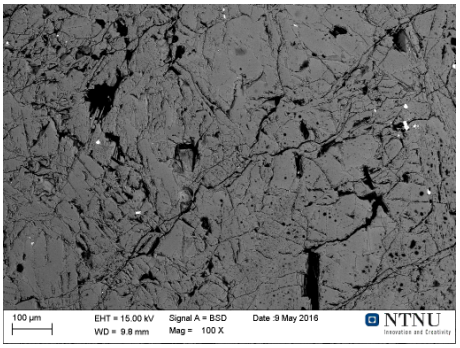

(a) 100x magnification **(b)** 500x magnification

Figure 5.11: SEM images of sample C-S

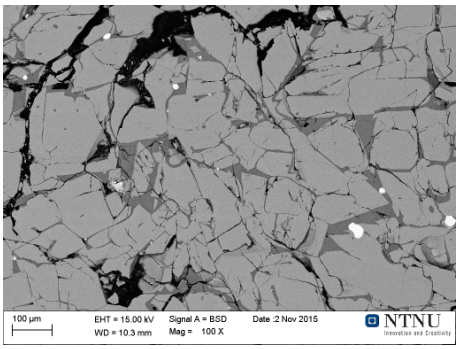

(a) At100 **(b)** Ac100

Figure 5.12: SEM images of samples S-At and S-Ac at 100x magnification

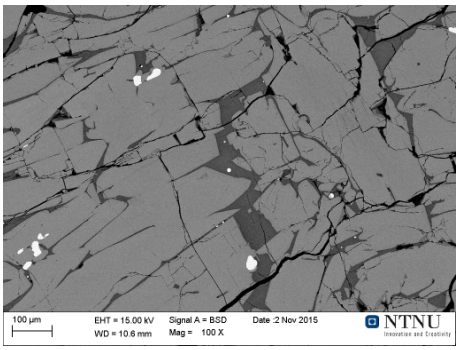

(a) At100 **(b)** Ac100

Figure 5.13: SEM images of samples S-Ab and S-Wt at 100x magnification

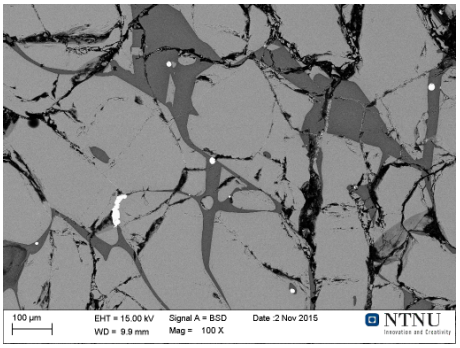

(a) At100 **(b)** Ac100

Figure 5.14: SEM images of samples S-Wc and S-Wb at 100x magnification

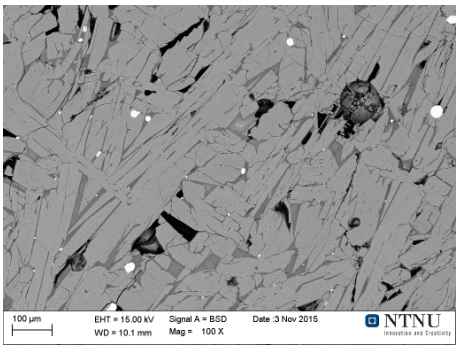

Figure 5.15: SEM image of sample S-S at 100x magnification

5.2 EDS analysis

The results from the EDS analysis is given in Figures 5.16 through 5.25. In the element content tables, the legends are as follows: The main titanium phase is marked as *Ti#1*, the secondary titanium phase (of present) is marked as *Ti#2*, the iron globules are marked as *Fe#1* and the glassy silicon phase is marked as *Si#1*. If a given phase is not present in the sample analyzed, the name is marked with a strike-through.

The element contents are rounded to two significant figures for easier readability.

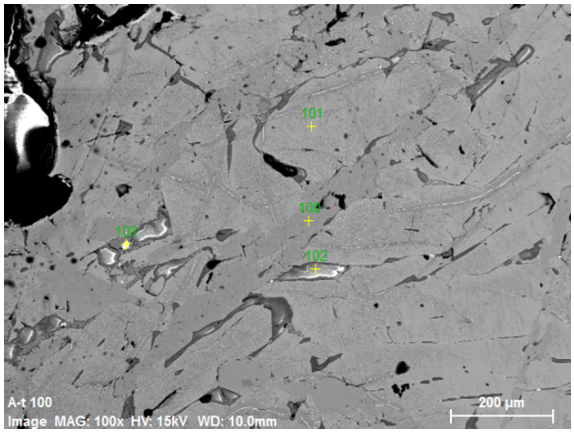

	Ti#1	Ti#2	Fe#1	Si#1
Ti	34	37	1.8	2.4
Fe	4.5	-	92	0.62
Si	-	-	-	25
O	56	60	-	63
C	2.5	2.9	5.9	-
Al	1.2	-	-	3.4
Mg	1.1	-	-	-
Mn	0.55	-	-	0.46
Na	-	-	-	2.1
Ca	-	-	-	1.4
K	-	-	-	0.59
Br	-	-	-	-

(a) Phases analyzed **(b)** Element contents

Figure 5.16: EDS analysis of sample C-At

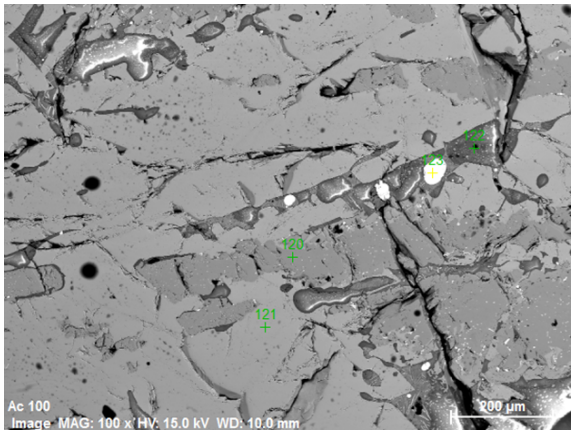

	Ti#1	Ti#2	Fe#1	Si#1
Ti	35	40	-	1.5
Fe	6.2	-	92	0.58
Si	-	-	-	37
O	54	60	2.7	50
C	2.4	-	4.7	-
Al	1.2	-	-	4.2
Mg	0.92	-	-	-
Mn	0.90	-	-	0.63
Na	-	-	-	2.8
Ca	-	-	-	1.8
K	-	-	-	1.8
Br	-	-	-	-

(a) Phases analyzed **(b)** Element contents

Figure 5.17: EDS analysis of sample C-Ac

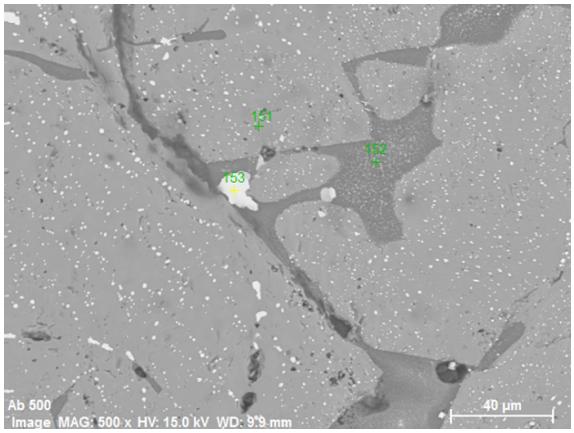

(a) Phases analyzed

	Ti#1	~~Ti#2~~	Fe#1	Si#1
Ti	31	-	2.1	2.3
Fe	2.1	-	83	2.6
Si	-	-	-	26
O	51	-	-	53
C	9.6	-	13	7.7
Al	-	-	-	3.9
Mg	3.1	-	-	-
Mn	2.7	-	-	0.42
Na	-	-	1.6	0.51
Ca	-	-	-	2.3
K	-	-	-	-
Br	1.1	-	-	-

(b) Element contents

Figure 5.18: EDS analysis of sample C-Ab

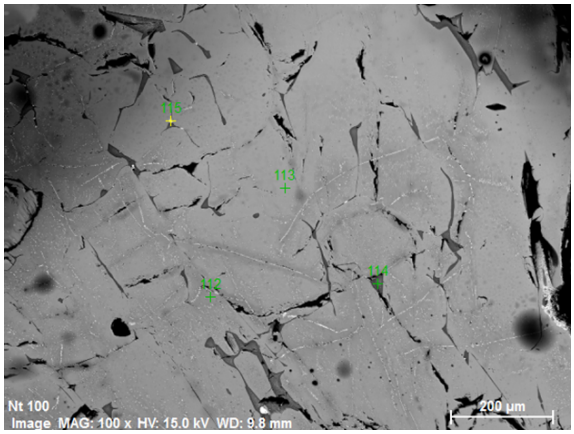

(a) Phases analyzed

	Ti#1	~~Ti#2~~	Fe#1	Si#1
Ti	39	-	2.9	2.1
Fe	-	-	81	0.26
Si	-	-	-	32
O	55	-	-	56
C	2.7	-	6.9	-
Al	1.6	-	5.3	5.7
Mg	1.1	-	-	-
Mn	0.68	-	-	0.21
Na	-	-	-	1.0
Ca	-	-	-	2.3
K	-	-	-	0.64
Br	-	-	4.0	-

(b) Element contents

Figure 5.19: EDS analysis of sample C-Wt

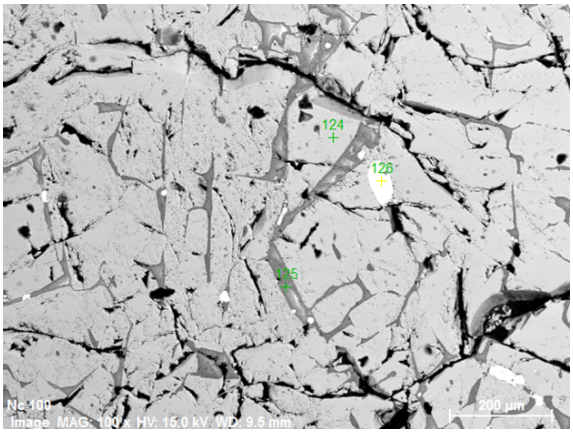

	Ti#1	~~Ti#2~~	Fe#1	Si#1
Ti	36	-	-	1.4
Fe	6.0	-	89	0.50
Si	-	-	-	29
O	53	-	2.7	54
C	2.3	-	8.0	6.3
Al	1.3	-	-	4.5
Mg	0.83	-	-	-
Mn	0.82	-	-	0.81
Na	-	-	-	0.75
Ca	-	-	-	2.6
K	-	-	-	-
Br	-	-	-	-

(a) Phases analyzed **(b)** Element contents

Figure 5.20: EDS analysis of sample C-Wc

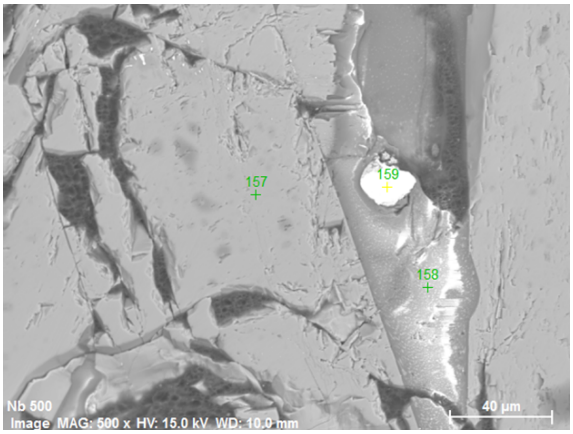

	Ti#1	~~Ti#2~~	Fe#1	Si#1
Ti	37	-	0.89	1.3
Fe	4.1	-	91	0.22
Si	-	-	-	24
O	57	-	-	59
C	-	-	8.5	7.4
Al	-	-	-	4.0
Mg	0.89	-	-	-
Mn	-	-	-	0.26
Na	-	-	-	0.64
Ca	-	-	-	2.4
K	-	-	-	-
Br	0.76	-	-	-

(a) Phases analyzed **(b)** Element contents

Figure 5.21: EDS analysis of sample C-Wb

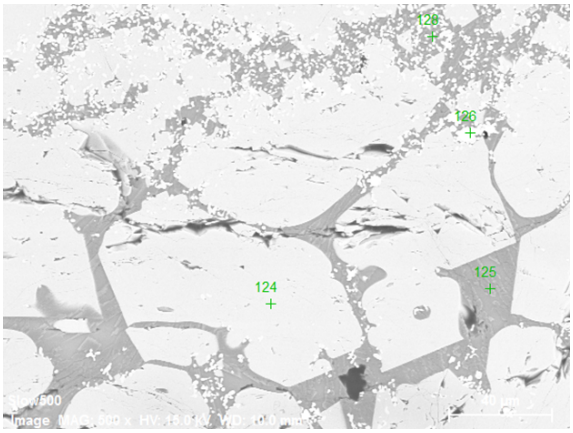

	Ti#1	~~Ti#2~~	Fe#1	Si#1
Ti	33	-	2.1	2.1
Fe	-	-	62	-
Si	-	-	-	16
O	51	-	-	48
C	11.2	-	36	17
Al	0.54	-	-	3.1
Mg	3.8	-	-	10
Mn	-	-	-	0.52
Na	-	-	-	-
Ca	-	-	-	2.5
K	-	-	-	-
Br	-	-	-	-

(a) Phases analyzed **(b)** Element contents

Figure 5.22: EDS analysis of sample IF-Slow

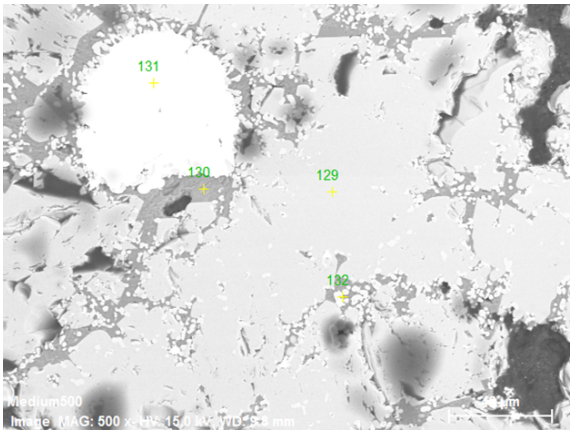

	Ti#1	~~Ti#2~~	Fe#1	Si#1
Ti	33	-	0.46	2.4
Fe	-	-	68	-
Si	-	-	3.5	16
O	51	-	-	51
C	12	-	25	14
Al	1.6	-	2.8	3.9
Mg	3.5	-	-	7.1
Mn	-	-	-	0.52
Na	-	-	-	-
Ca	-	-	-	4.7
K	-	-	-	-
Br	-	-	-	-

(a) Phases analyzed **(b)** Element contents

Figure 5.23: EDS analysis of sample IF-Medium

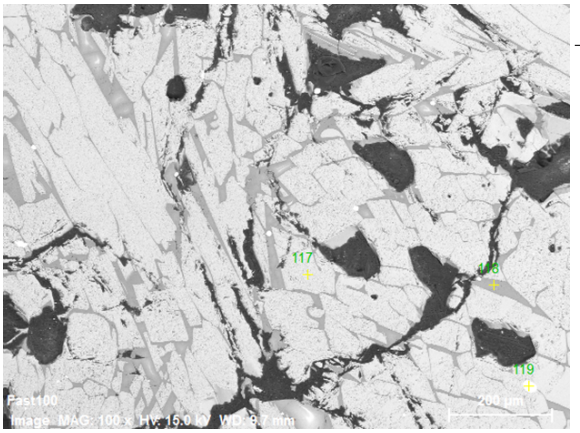

(a) Phases analyzed

	Ti#1	~~Ti#2~~	Fe#1	Si#1
Ti	36	-	1.8	2.4
Fe	0.67	-	75	0.88
Si	-	-	-	21
O	51	-	-	54
C	9.4	-	23	-
Al	0.83	-	-	4.0
Mg	2.4	-	-	10
Mn	-	-	-	1.3
Na	-	-	-	2.5
Ca	-	-	-	2.9
K	-	-	-	-
Br	-	-	-	-

(b) Element contents

Figure 5.24: EDS analysis of sample IF-Fast

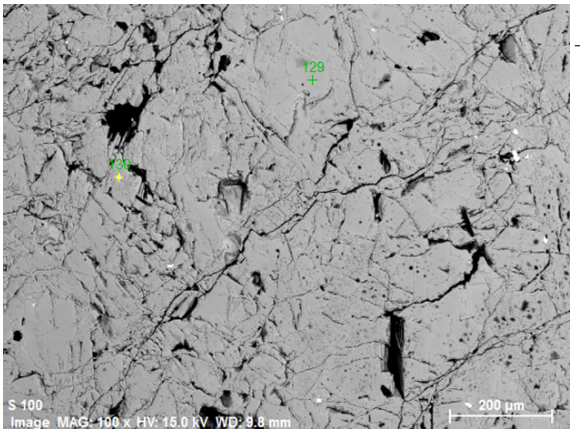

(a) Phases analyzed

	Ti#1	~~Ti#2~~	Fe#1	~~Si#1~~
Ti	38	-	2.4	-
Fe	1.4	-	92	-
Si	-	-	-	-
O	52	-	-	-
C	6.1	-	4.2	-
Al	1.4	-	1.1	-
Mg	1.1	-	-	-
Mn	-	-	-	-
Na	-	-	-	-
Ca	-	-	-	-
K	-	-	-	-
Br	-	-	-	-

(b) Element contents

Figure 5.25: EDS analysis of sample C-S

5.3 XRD analysis

The XRD results are given in Figures 5.26 through 5.35. The spectras have been matched against database values, and the peaks marked according to the phase it originates from.

A summary of the phases found in the samples are given in Table 5.1.

	C-At	C-Ac	C-Ab	C-Nt	C-Nc	C-Nb	Slow	Medium	Fast	C-S
Rutile	**main**	trace	**main**	trace	trace	trace	trace	trace	-	trace
P.brookite	**main**	**main**	**main**	**main**	**main**	**main**	-	-	**main**	**main**
Anatase	-	trace	trace	trace	trace	trace	-	-	trace	trace
Wuestite	-	-	-	-	-	-	trace	trace	trace	-
Graphite	-	-	-	-	-	-	trace	trace	trace	-
FeO_3Ti	-	-	-	-	-	-	**main**	**main**	trace	-

Table 5.1: Summary of XRD results given as phases identified in the samples. Phases with large signals are marked as "**main**", while phases with weak signals are marked as "trace"

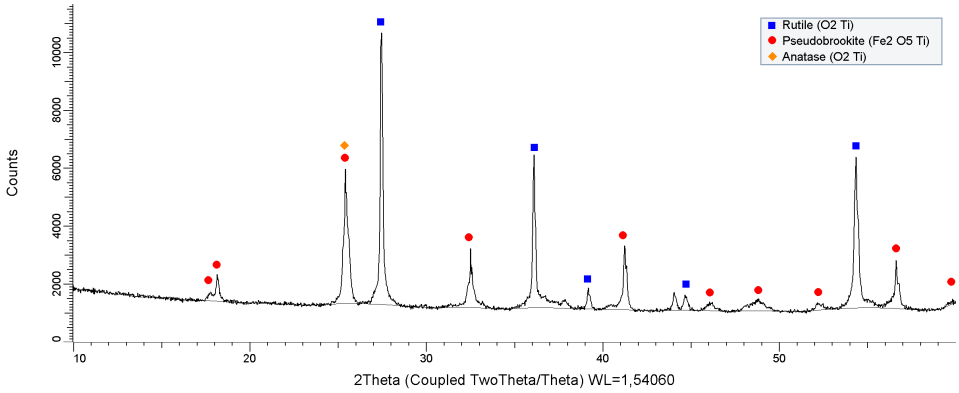

Figure 5.26: XRD diagram of sample C-At

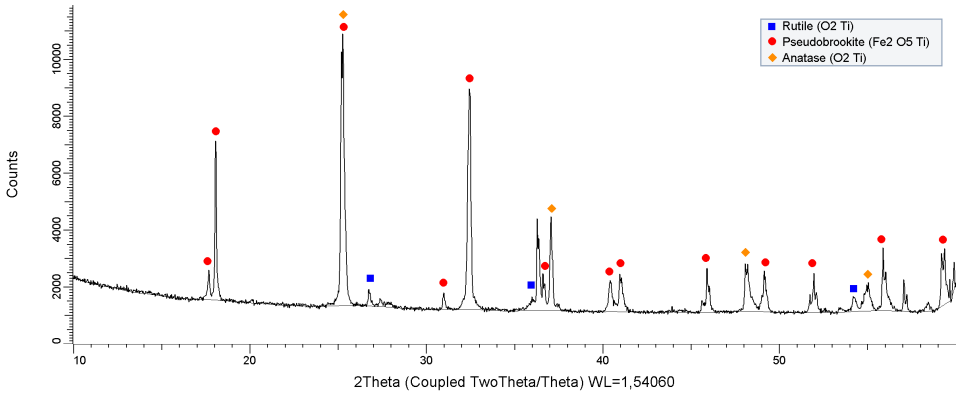

Figure 5.27: XRD diagram of sample C-Ac

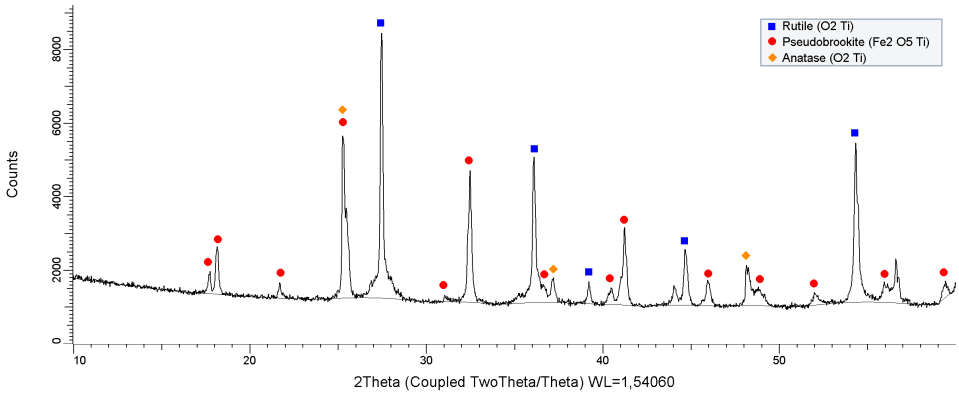

Figure 5.28: XRD diagram of sample C-Ab

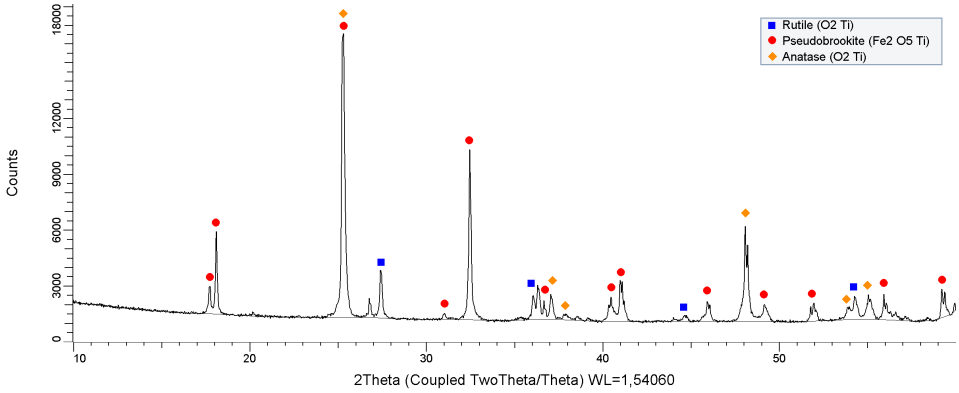

Figure 5.29: XRD diagram of sample C-Wt

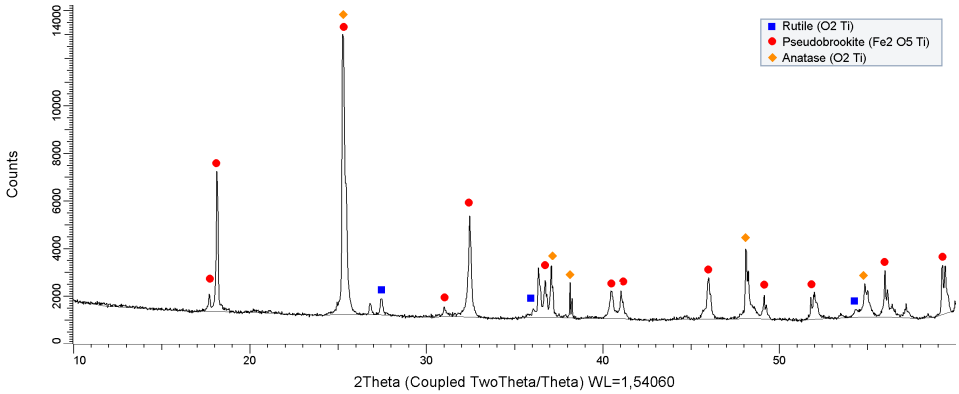

Figure 5.30: XRD diagram of sample C-Wc

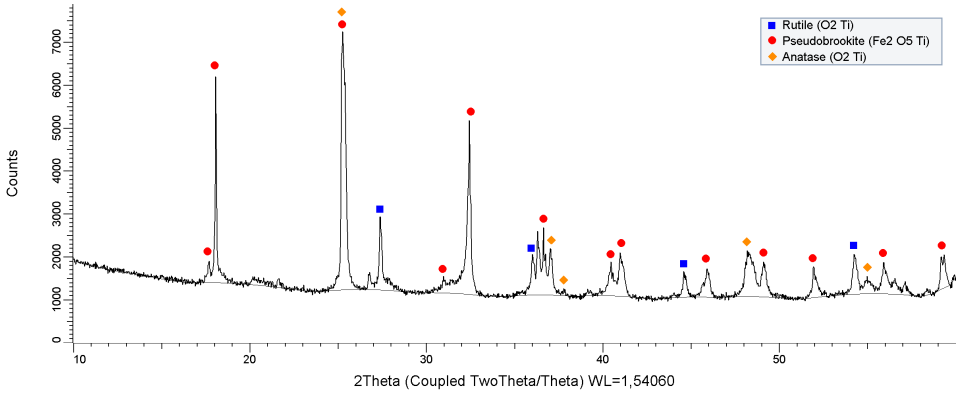

Figure 5.31: XRD diagram of sample C-Wb

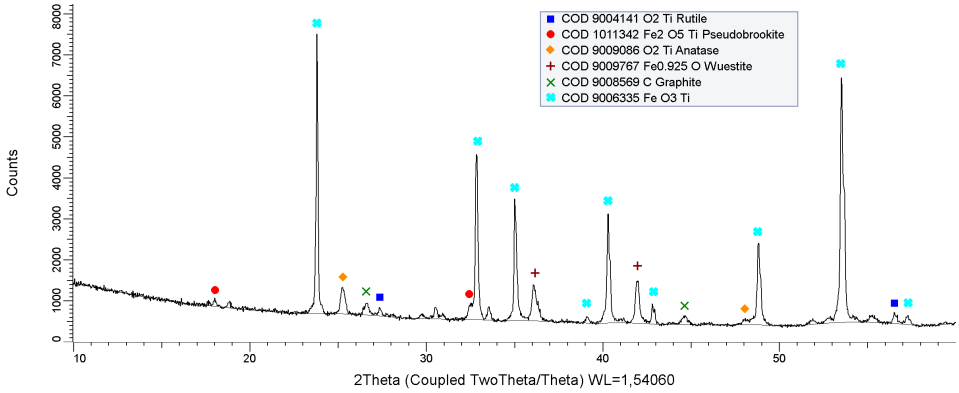

Figure 5.32: XRD diagram of sample IF-slow

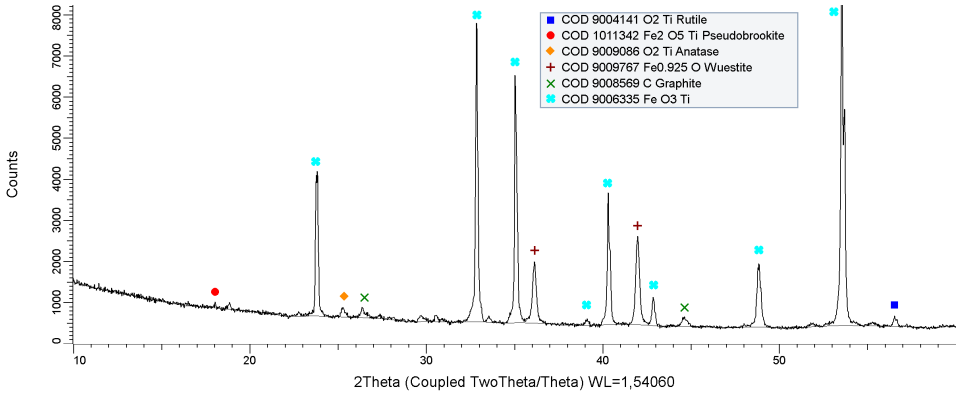

Figure 5.33: XRD diagram of sample IF-medium

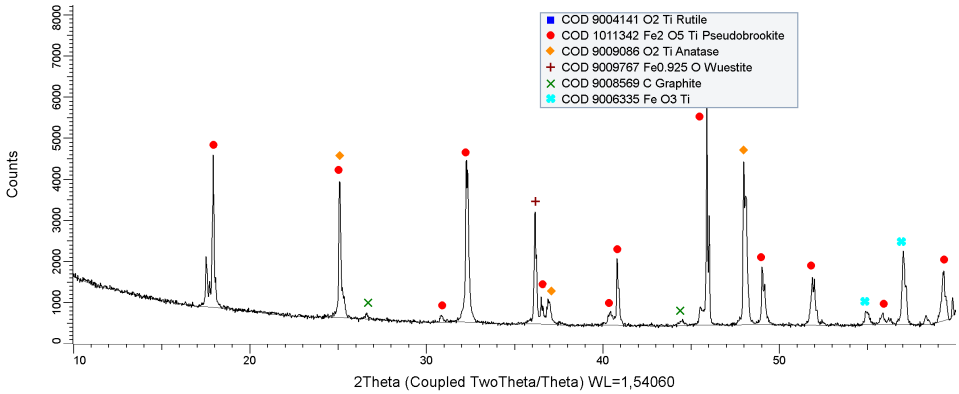

Figure 5.34: XRD diagram of sample IF-fast

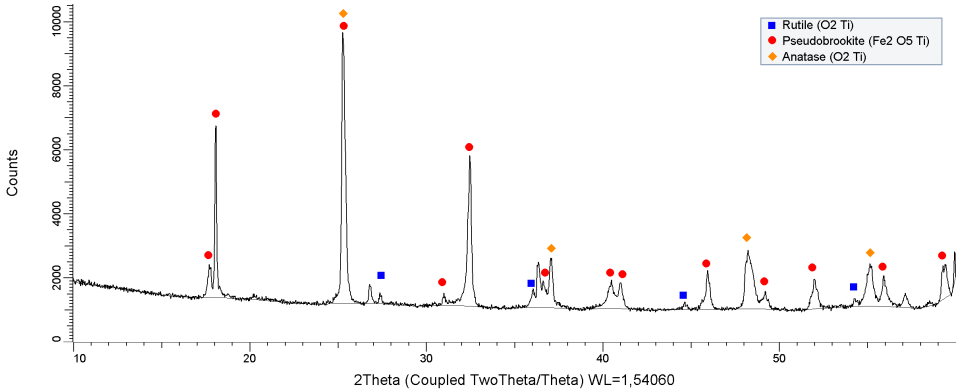

Figure 5.35: XRD diagram of sample C-S

5.4 Thermal expansion

Due to apparatus downtime and time restraints, thermal expansion readings were acquired for only one of the samples in the set. The result from the dilatometer test on sample *C-Wt* is given in Figure 5.36.

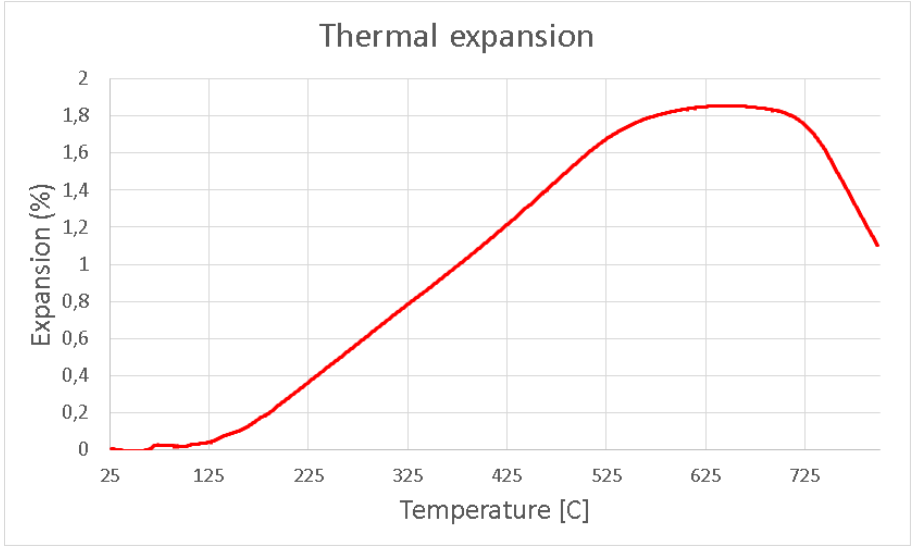

Figure 5.36: Thermal expansion of the sample *C-Wt* pressed from powders of particle size $<71\,\mu m$

5.5 Laser flash analysis

For the same reasons as the lack of thermal expansion data, the results of the completed laser flash analysis have not been retrievable. The results in this section is therefore completely lacking.

Chapter 6

Discussion

6.1 Grain size

This section will overview the differences observed in grain size of the different samples, and relate this to what was previously predicted about the cooling rates of the samples. It is also useful to be able to relate the cooling rates of the industrially collected samples to the experimentally prepared samples. This is mainly because the experimentally prepared samples have corresponding measured temperature profiles, but the industrial samples do not.

During the original sample gathering, the cooling rates of the samples were predicted in the following order, from fast to slow:

- Tapping stream sample → Water cooled cake → Air cooled cake

and within the slag cakes, the cooling is arranged from fast to slow:

- Top → Bottom → Center

The predicted relative cooling rates ought to conform to a pseudobrookite grain size from small to big in the same order. How does this hold up for the samples analyzed?

In general, the air cooled samples have larger grains than the water cooled samples. The tapping stream sample exhibits a much smaller grains size than the other industrially collected samples. This is all as expected. The comparison of the tapping stream sample and the two center samples are shown in Figure 6.1.

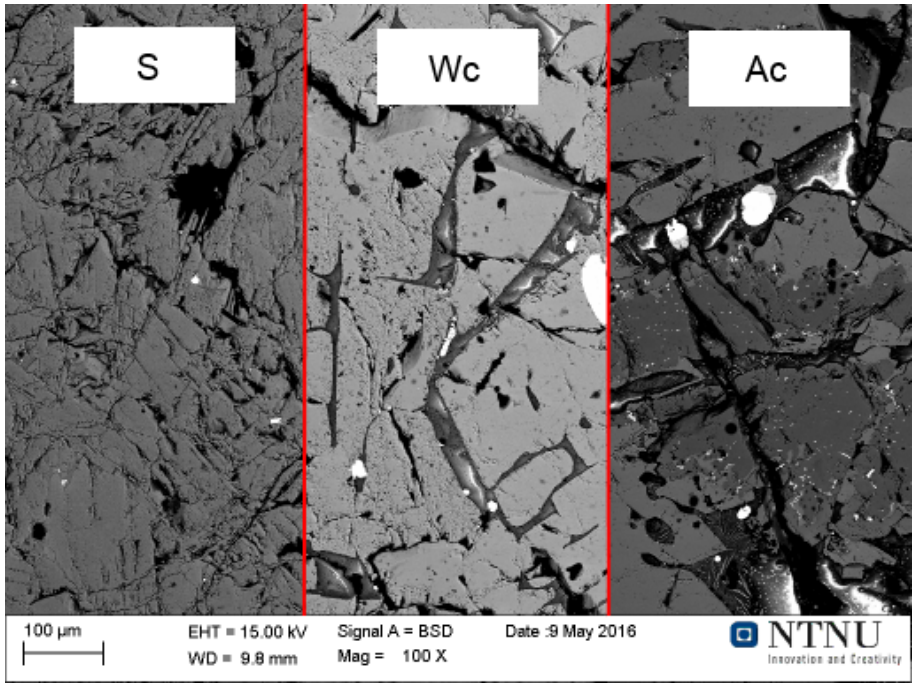

Figure 6.1: Comparison of grain size of the tapping stream sample and the two center samples from the slag cakes (C-S, C-Wc and C-Ac)

However, there is very little difference between the grain sizes of the samples collected at different places from the same cake. The top, center and bottom samples of the water cooled cake shows a very similar grain size. This is also the case within the air cooled cake. This indicates that the cooling rates between the samples taken at different places within the same cake are smaller than previously expected.

The samples prepared in the furnace experiments all have small grain sizes compared to the industrially collected samples from the slag cakes. This indicates that all three cooling rates applied to the furnace samples are actually faster than the different rates experienced by the industrial samples, excluding the very rapid tapping stream sample. In future experiments, it is therefore advisable that cooling time of the experimentally prepared samples be increased even further.

The grain sizes in the three experimentally produced samples do not vary much between the samples. This indicates that although the produced samples have cooling times ranging from $30\,\mathrm{min}$ to $180\,\mathrm{min}$ between the temperatures $1600\,^{\circ}\mathrm{C}$ and $400\,^{\circ}\mathrm{C}$, the cooling rate difference is not large enough to facilitate great differences in solidification. This also points towards larger differences in cooling when producing samples experimentally.

6.2 EDS element analysis

In Section 2.3.2, it is explained how the pseudobrookite phase will correspond to the structure M_3O_5 where M will include varying amounts of Ti, Fe and Mg. It is also very likely to contain a mixture of the elements Al, Mn, Ca, and Cr.

The TiO_2 phases (mainly rutile and anatase as seen by the XRD results) are pure phases and will contain none or few elements other than Ti and O. The glassy Si-rich phase, however, contains a plethora of trace elements.

This information has been used when describing the phases present from the EDS results. All samples contain a Ti phase with plenty of trace elements: This is the pseudobrookite phase. Only two of the samples (C-At and C-Ac) exhibits a distinguishable pure Ti-O phase. These are assumed to be the rutile phase.

The phases in the IF75 prepared samples have a generally higher carbon content than the phases in the industrially collected samples. This is owed to the carbon crucible used in the melting experiments, and the high reactivity of the slag in its molten form.

6.3 Phases present

One of the main aspects to be drawn from the Introduction chapter is the importance of the rutile phase. This section will look at the presence of this phase, together with the other phases present in the samples.

6.3.1 Pseudobrookite

From Table 5.1 in Section 5.3, it is evident that the pseudobrookite phase is the primary phase in the titanium slag, as expected. Major pseudobrookite peaks are present in the XRD spectras of *almost* all the samples.

The two experimentally produced samples *IF-Slow* and *IF-Medium* are the only samples without major pseudobrookite peaks in the XRD spectras, and these do not contain the pseudobrookite peaks at all. Instead, these two samples gives rise to major $FeTiO_3$ (ilmenite) peaks. These samples also show traces of FeO (wuestite).

The lack of pseudobrookite in these samples, together with the presence of ilmenite, may be explained in the following way. The experimentally produced samples are prepared from an industrial slag, *not* from an ilmenite ore. The original slag contains some amounts of rutile, which has a melting point of more than $1800\,^{\circ}\mathrm{C}$. This means that during the melting of the slag, the rutile contents of the original slag may not have completely melted, shifting the elemental contents of the produced melt.

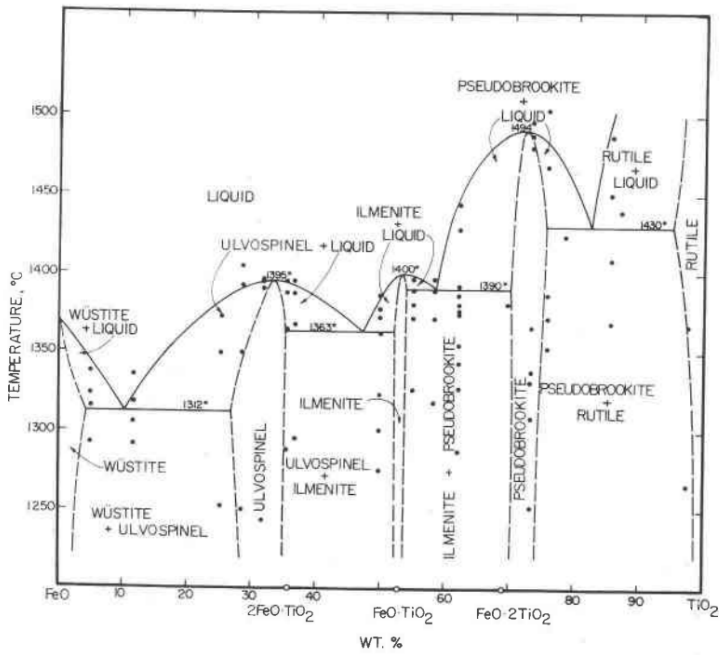

Figure 6.2: The FeO - TiO_2 binary phase diagram [27]

The binary phase diagram FeO - TiO_2 as proposed by *MacChesney* and *Muan* is shown in Figure 6.2 [27]. From the diagram, it suggests that the contents of the melt could be skewed towards the ilmenite region, away from the pseduobrookite region. This does, however, seem very unlikely because of the relative low amounts of rutile formed in the original slag as previously shown in Table 4.3.

6.3.2 Wuestite

The three samples produced in the IF75 furnace show traces of wuestite (FeO_x). This does not come as a surprise, as the chemical analysis in Tables 4.2 and 4.4 indicate FeO amounts between 8% and 10% in all the samples. The question that needs answering is then: Why is there no wuestite signal in the industrially collected samples? This is simply answered by the fact that the major wuestite peak in the XRD diagram coincides exactly with one of the major rutile peaks. Coupling this together with the FeO contents reported in the chemical analysis makes it highly likely that there are wuestite signals in all the samples, but they are overshadowed by the rutile peak.

6.3.3 Graphite

The XRD results also show graphite contents in the IF75 prepared samples, but not in the industrially collected ones. This is explained as introduced by the carbon crucibles used in the melting experiments.

6.3.4 Anatase

There are traces of anatase in most of the industrially collected samples, and in one of the experimentally prepared ones. As previously explained in Section 2.3.3, anatase is a metastable polymorph of TiO_2. It transforms to rutile between the temperatures 600 °C and 1100 °C.

The simplest way of explaining anatase contents in the slag would be as such: If the slag is held at an appreciable amount of time between 600 °C and 1100 °C, anatase will transform to the thermodynamically stable polymorph rutile. The results from the XRD scans seem to contradict this, as anatase is present in the slower cooled samples, but not in the quicker ones. But rather than a contradiction to the theory, it is explained by the lack of formation of *both* forms of TiO_2 in the quickly cooled samples.

The traces of anatase seen in the industrially collected samples are then seen as formed by the same mechanisms as the rutile. While some of it would have transformed to rutile in the temperature interval given, some of it still remain.

6.3.5 Rutile

The XRD results show rutile contents in all samples except the quickly cooled IF75 prepared sample. According to the theory, rutile is formed from pseudobrookite at elevated temperatures during cooling. Quickly cooling past these temperatures will then limit the amount of rutile formed. The quickly cooled IF75 sample has arguably the highest cooling rate of all the samples in the set, so the lack of rutile is readily explained.

The rutile peaks in the XRD scans for the two samples C-At and C-Ab (the top and bottom of the air cooled slag cake) are significantly more pronounced, indicating a higher rutile content in these two samples. In the SEM pictures the samples C-At and C-Ac (top and center) shows rutile phases. This is shown in Figure 6.3.

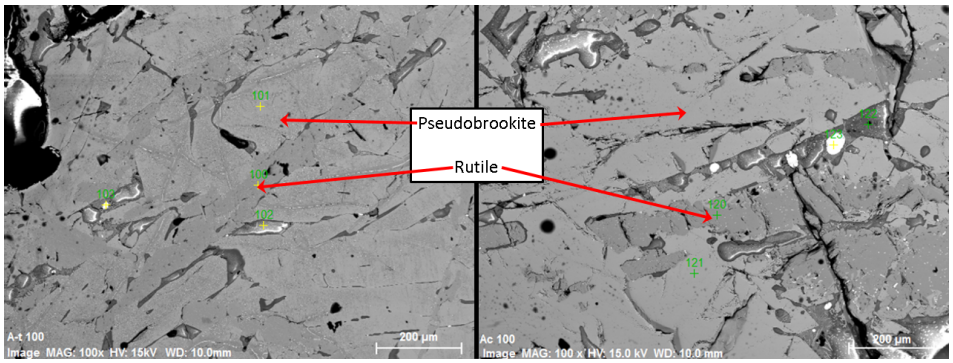

Figure 6.3: Rutile contents of the two samples C-At and C-Ac. These two samples are the only ones in the set where rutile is identified in the SEM pictures. C-At on the left, C-Ac on the right

Because the air cooled cake samples had the slowest cooling rates of all samples in the set, a higher rutile content is expected. It is then interesting to note that the center and bottom samples, which experienced slower cooling rates than the top sample, show

lower rutile contents (only one of them has rutile in the picture, while the other has more pronounced XRD peaks). The lower rutile content may be explained by the poor access to oxygen in the center and bottom of the sample.

The decomposition of pseudobrookite to rutile in Equation 6.1 generally has a hard time nucleating the two new phases (metallic iron and rutile) before some oxidation of the slag has occurred [28]. Although the decomposition reaction itself does not require external oxygen, it may still require some to start off the reaction.

$$FeTi_2O_5 + Ti_3O_5 \rightarrow Fe + 5TiO_2 \tag{6.1}$$

Chapter 7

Conclusion

7.1 Cooling rates

When collecting the industrial samples, they were chosen in such a way that they would receive different cooling rates. These rates were then estimated relative to each other as previously described. When samples were prepared experimentally in the university, the cooling rates were meticulously measured. One of the goals of this thesis was to relate the exactly measured cooling rates of these experimentally prepared samples to the industrially collected ones.

The result of this, is that all the experimentally prepared samples had cooling rates faster than the samples from the industrial slag cakes. This is not what was originally intended, but it is so. It will then be useful to prepare slags of even slower cooling rates to match those of the industrial process.

7.2 Phase composition

The main phase identified in the samples were the pseudobrookite phase, as was expected from the relevant theory and literature review. Some of the experimentally prepared samples showed deviations from this, because their arguably differences in environment during cooling such as high oxygen and carbon availability and fast cooling rates.

Rutile phases was primarily identified in the industrially collected samples from the air cooled slag cake. Compared to the water cooled slag cake, these samples had both slower cooling rates and better access to oxygen after tapping from the furnace. The rutile contents identified are therefore in accordance with the theory presented.

7.3 Further work

Firstly, preparing samples with cooling rates closer to those of the industrial process is of importance. To get a closer match in cooling conditions, both higher slag quantities

and better insulation is required when preparing the samples. Eliminating the carbon contamination from the carbon crucible would also aid in preparing samples closer to those collected industrially. This can for example be achieved by using a cold-crucible setup instead of the carbon crucible.

Secondly, completing the analysis of thermal properties of the slag will be interesting. The difference in thermal conductivity and heat capacity (if any) of the different slag samples will provide a solid quantitative data set on the solid slag.

In addition to this, knowing the thermal properties of the solid slag will aid in the understanding of currently used industrial furnaces, as these operate with a solid slag freeze lining. The thermal conductivity and heat capacity of the slag lining are used as parameters when modelling the furnace, so a thorough understanding of these values will yield more accurate models.

Bibliography

[1] R. G. Becher, R. G Canning, B. A Goodheart, and S. Uusna. A new process for upgrading ilmenitic mineral sands. *Australasian Institute of Mining and Metallurgy - Proceedings*, 214:21–44, 1965.

[2] Stephen C. Lobo. Experimental investigations and modelling of solid-state ilmenite rediction with hydrogen and carbon monoxide. 2015.

[3] Terkel Rosenqvist, Johan Kr Tuset, Sverre E. Olsen, and institutt Norges tekniske hgskole Metallurgisk. *Terkel Rosenqvist Symposium : proceedings of the international symposium arranged in honour of Terkel Rosenqvist, the Norwegian Institute of Technology, Trondheim, May 8-11, 1988*. Norges tekniske hgskole, Division of Metallurgy, Trondheim, 1988.

[4] NETZSCH. Principle of the lfa method. `https://www.netzsch-thermal-analysis.com/en/landing-pages/principle-of-the-lfa-method/`, 2016.

[5] R. W. Taylor. Phase equilibriums in the system feo-fe2o3-tio2 at 1300. *Am. Mineral.*, 49:1016–30, 1964. CAPLUS AN 1965:12492(Journal).

[6] John F. W. Bowles. Definition and range of composition of naturally occurring minerals with the pseudobrookite structure. *American Mineralogist*, 73(11):1377–1383, 1988.

[7] A. Przepiera and M. Jaboski. Thermal transformations of titanium slag of high titania content. *Journal of Thermal Analysis and Calorimetry*, 74(2):631–637, 2003.

[8] Ivo Toromanoff and Fathi Habashi. The composition of a titanium slag from sorel. *J. Less-Common Met.*, 97:317–29, 1984. CAPLUS AN 1984:142807(Journal).

[9] Michal Ksiazek. The thermophysical properties of raw materials for ferromanganese production. 2012.

[10] Tomohiro Akiyama, Hiromichi Ohta, Reijiro Takahashi, Yoshio Waseda, and Junichiro Yagi. Measurement and modeling of thermal conductivity for dense iron oxide and porous iron ore agglomerates in stepwise reduction. *ISIJ International*, 32(7):829–837, 1992.

[11] G. M Bedinger. U.s geological survey, mineral commodity summaries, titanium mineral concentrates. 2014.

[12] Terkel Rosenqvist. Ilmenite smelting. *Transactions of the Technical Univeristy of Kosice*, 2(40-46), 1992.

[13] T. S. Mackey. Acid leaching of ilmenite into synthetic rutile. *Industrial and Engineering Chemistry Product Research and Development*, 13(1):9–18, 1974.

[14] Thomas P. Battle, Dat Nguyen, and James W. Reeves. The processing of titanium-containing ores. volume 1, pages 925–43. Miner. Met. Mater. Soc., 1993. CAPLUS AN 1993:258465(Conference; General Review).

[15] R. Byron Bird, Warren E. Stewart, and Edwin N. Lightfoot. *Transport Phenomena, 2nd Edition*. Wiley, 2001.

[16] William D. Callister and David G. Rethwisch. *Materials science and engineering : an introduction*. Wiley, New York, 7th ed. edition, 2007.

[17] Jarle Hjelen. Scanning elektron-mikroskopi, 1986.

[18] Anthony R. West. *Basic Solid State Chemistry*. John Wiley & Sons Ltd., 2 edition, 1999.

[19] T. Baba, M. Kobayashi, A. Ono, J. H. Hong, and M. M. Suliyanti. Experimental investigation of the nonuniform heating effect in laser flash thermal diffusivity measurements. *Thermochimica Acta*, 218:329–339, 1993.

[20] D. Bessinger, J. M. A. Geldenhuis, P. C. Pistorius, A. Mulaba, and G. Hearne. The decrepitation of solidified high titania slags. *J. Non-Cryst. Solids*, 282(1):132–142, 2001. CAPLUS AN 2001:379853(Journal).

[21] Ay Medvedev. Synthetic armalcolite and pseudobrookite. *Mineral. Mag.*, 60(399):347–353, 1996.

[22] A. T. Anderson, T. E. Bunch, and E. N. Cameron. Armalcolite: A new mineral from the apollo 11 samples. *Proceedings of the Apollo 11 Lunar Science Conference*, 1:55–63, 1970.

[23] *Earth Sciences in the 21st Century : Rutile: Properties, Synthesis and Applications : Properties, Synthesis and Applications*. Nova, Hauppauge, US, 2012.

[24] Ji-Guang Li and Takamasa Ishigaki. Brookite rutile phase transformation of tio 2 studied with monodispersed particles. *Acta Materialia*, 52(17):5143–5150, 2004.

[25] James Ovenstone and Kazumichi Yanagisawa. Effect of hydrothermal treatment of amorphous titania on the phase change from anatase to rutile during calcination. *Chemistry of Materials*, 11(10):2770–2774, 1999.

[26] Rune H. Stana. Solidification of slags and influence on post processing, 2015.

[27] J. B. MacChesney and Arnulf Muan. Phase equilibria at liquidus temperatures in the system iron oxide-titanium oxide at low oxygen pressures. *American Mineralogist*, 46:572–582, 1961.

[28] P. C. Pistorius. Ilmenite smelting: the basics. *J. S. Afr. Inst. Min. Metall.*, 108(1):35–43, 2008.